DOI: https://doi.org/10.2138/am-2020-7075

Revision 2

Elasticity of single-crystal Fe-enriched diopside at high-pressure conditions: Implications for the cause of upper mantle low-velocity zones

DAWEI FAN[1,2,*], SUYU FU[2], CHANG LU[2], JINGUI XU[1], YANYAO ZHANG[2], SERGEY N. TKACHEV[3], VITALI B. PRAKAPENKA[3], JUNG-FU LIN[2,*]

[1]Key Laboratory of High-Temperature and High-Pressure Study of the Earth's Interior, Institute of Geochemistry, Chinese Academy of Sciences, Guiyang, Guizhou 550081, China

[2]Department of Geological Sciences, Jackson School of Geosciences, The University of Texas at Austin, Austin, Texas 78712, USA

[3]Center for Advanced Radiation Sources, University of Chicago, Chicago, Illinois 60437, USA

[*]Email: fandawei@vip.gyig.ac.cn; afu@jsg.utexas.edu

Abstract:

Diopside is one of the most important end-members of clinopyroxene, which is an abundant mineral in upper-mantle petrologic models. The amount of clinopyroxene in upper-mantle pyrolite can be ~15 vol.% while pyroxenite can contain as high as ~60 vol.% clinopyroxene. Knowing the elastic properties of the upper-mantle diopside at high pressure-temperature conditions is then essential for constraining the chemical composition and interpreting seismic observations of region. Here we have measured the single-crystal elasticity of Fe-enriched diopside ($Di_{80}Hd_{20}$, Di-diopside, and Hd-hedenbergite; also called Fe-enriched clinopyroxene) at high-pressure conditions up to 18.5 GPa by using *in situ* Brillouin light scattering spectroscopy (BLS) and synchrotron X-ray diffraction in the diamond anvil cell. Our experimental results were used in evaluating the effects of pressure and Fe substitution on the full single-crystal elastic moduli across the Di-Hd solid solution series to better understand the seismic velocity profiles of the upper mantle. Using the third- or fourth-order Eulerian finite-strain equations of state to model the elasticity data, the derived aggregate adiabatic bulk and shear moduli (K_{S0}, G_0) at ambient conditions were 117(2) and 70(1) GPa, respectively. The first- and second-pressure derivatives of bulk and shear moduli at 300 K were $(\partial K_S/\partial P)_T$=5.0(2), $(\partial^2 K_S/\partial P^2)_T$=-0.12(4) GPa^{-1} and $(\partial G/\partial P)_T$=1.72(9), $(\partial^2 G/\partial P^2)_T$=-0.05(2) GPa^{-1}, respectively. A comparison of our results with previous studies on end-member diopside and hedenbergite in the literatures shows systematic linear correlations between the Fe composition and single-crystal elastic moduli. An addition of 20 mol.% Fe in diopside increases K_{S0} by ~1.7% (~2 GPa) and reduces G_0 by ~4.1% (~3 GPa), but has a negligible effect on the pressure derivatives of the bulk and shear moduli within experimental uncertainties. In addition, our modelling results show that substitution of 20 mol.% Fe in diopside can reduce V_P and V_S by ~1.8% and ~3.5%, respectively along both an expected normal mantle geotherm and a representative cold subducted slab geotherm. Furthermore, our modelling results also show that the V_P and V_S profiles of Fe-enriched pyroxenite along the cold subducted slab geotherm are ~3.2% and ~2.5% lower than AK135 model at 400 km depth, respectively. Finally, we propose that the presence of Fe-enriched pyroxenite (including Fe-enriched clinopyroxene, Fe-enriched orthopyroxene, and Fe-enriched olivine), can be an effective mechanism to cause low-velocity anomalies in the upper mantle regions atop the 410-km discontinuity at cold subudcted slab conditions.

Keywords: Fe-enriched diopside, Single-crystal elasticity, Brillouin light scattering, high pressure, Low-velocity zone, 410-km discontinuity

INTRODUCTION

Ca-rich clinopyroxene (Cpx) in the Di-Hd solid solution series is one of the most abundant constituent minerals in the upper mantle, along with olivine, orthopyroxene (Opx), and pyrope-rich garnet (Fumagalli and Klemme 2015). The volumetric proportion of Cpx is in the range of ~15-75 vol.% depending on its mineralogical abundance in different rock types (Duffy and Anderson 1989; Ringwood 1991). For example, mantle-derived peridotite commonly contain ~15 vol.% Cpx (e.g. Davis et al. 2009; Takazawa et al. 2000), while mantle-derived pyroxenite xenoliths in alkali basaltic or kimberlitic lavas contain up to ~60 vol.% Cpx (e.g. Lambart et al. 2013; Yang et al. 2016). As the most abundant end-member of Cpx in the deep Earth (Ringwood 1982), previous phase transformation studies have indicated that monoclinic diopside ($CaMgSi_2O_6$) with *C2/c* space group at ambient conditions was thermodynamically stable up to ~18 GPa and 1400 K (e.g. Akaogi et al. 2004; Kim et al. 1994; Oguri et al. 1997). Furthermore, recent studies have also demonstrated that the dissolution of pyroxenes into majoritic garnet is slow in some subducted slabs (Nishi et al. 2013; van Mierlo et al. 2013) suggesting the presence of metastable pyroxene even below 660-km discontinuity (Bina et al. 2001; Fukao and Obayashi 2013; Xu et al. 2017, 2018). Diopside is thus believed to play an important role in our understanding of the geochemistry, seismic features and geodynamics of the upper mantle as well as the subducted slabs in the upper mantle region (Irifune et al. 2000; Putirka et al. 2011).

Seismological studies have identified the seismic anomalies including low-velocity zones at various depths in the upper mantle regions (e.g. Song et al. 2004; Tauzin et al. 2010; Vinnik and Farra 2007), such as the low-velocity zone (LVZ) atop the 410-km discontinuity. The LVZ atop the 410-km discontinuity is characterized by a ~1.0-5.0% V_P and ~1.5-6.5% V_S reduction with thickness ranging from ~20 km to ~100 km, with an average of ~60 km (e.g. Li et al. 2014; Tauzin et al. 2010, 2013; Vinnik and Farra, 2007). However, the potential causes of the LVZ atop the 410-km discontinuity have been debated. Some studies suggested partial melting (e.g. Song et al. 2004; Vinnik et al. 2010) and thermal anomalies (e.g. Morishige et al. 2010; Obayashi et al. 2006), whereas other investigations concluded that the LVZ might be due to difference in composition (e.g. Lee 2003; Stixrude and Lithgow-Bertelloni 2005). In this sense, reliable interpretation of the LVZ atop the 410-km discontinuity also requires detailed knowledge about the elastic moduli and velocities of expected constituent minerals at high pressure-temperature (*P*-*T*) conditions (Bass et al. 2008; Duffy and Ahrens 1992; Duffy and Anderson 1989).

Insofar, the static compression and equation of state studies of diopside have been widely carried out using X-ray diffraction (XRD) technique (e.g. Hu et al. 2017; Levien and Prewitt 1981; Thompson and Downs 2008; Tribaudino et al. 2000; Zhang et al. 1997; Zhao et al. 1998). On the other hand, the elastic moduli (adiabatic bulk and shear moduli) of Mg-end-member diopside (also called Fe-free diopside) were measured using ultrasonic interferometry (UI) (Liebermann and Mayson 1976) and impulsive stimulated scattering (Collins and Brown 1998) at ambient conditions, using BLS method up to 14 GPa (Sang and Bass 2014), and by a combined UI and XRD methods (Li and Neuville 2010) up to 8 GPa and 1073 K. In addition, single-crystal elastic moduli of (Fe, Cr)-bearing diopside were also conducted using resonance ultrasonic spectroscopy (Isaak and Ohno 2003; Isaak et al. 2006) up to 1300 K, whereas the wave velocities and single-crystal elastic moduli of Fe-end-member hedenbergite were measured by BLS method (Kandelin and Weidner 1988a) at ambient conditions. In general, BLS has been a key technique in both measuring the acoustic velocities of mantle minerals and deriving the full set of single-crystal elastic moduli (e.g. Bass and Zhang 2015; Fan et al. 2015; Fan et al. 2019b; Speziale et al. 2014; Yang et al. 2015). BLS technique is also very suitable for the velocity measurements of low-symmetry minerals because one can prepare multiple platelets of the crystal and measure their velocities as a function of the azimuthal angles to derive full set of elastic moduli (Mainprice 2015). That said, it is time-consuming and technically challenging to obtain precise single-crystal elastic moduli of Cpx at high *P*-*T* using BLS method, because 13 independent single-crystal elastic moduli are necessary to characterize completely its elastic properties (Kandelin and Weidner 1988a, 1988b; Levien et al. 1979; Sang et al. 2011; Hao et al. 2019a, 2019b). So far, the single-crystal elasticity measurements on monoclinic diopside using BLS have been primarily performed at ambient conditions (e.g. Levien et al. 1979; Sang et al. 2011). Theoretical simulations by Matsui and Busing (1984), Walker (2012) and Zou et al. (2018) have reported the single-crystal elasticity of Fe-free diopside at high *P*/*T* conditions, but relevant experimental studies of diopside or diopside-bearing omphacite at high *P*-*T* conditions are still limited (Hao et al. 2019b; Sang et al. 2014). Until now, only Sang and Bass (2014) and Hao et al. (2019b) measured the single-crystal elastic moduli of Fe-free diopside and diopside-bearing omphacite at high-pressure conditions using BLS method, respectively.

Natural diopside typically contains appreciable amounts of Fe (Azough and Freer, 2000), which forms as an important solid solution diopside-hedenbergite ($CaFeSi_2O_6$) (Di-Hd) join. As an example, Cpx in the upper-mantle peridotite typically contains ~10 mol.% of Fe (e.g. Luth and Canil 1993; Woodland 2009), while Cpx in pyroxenite even can contains ~25 mol.% Fe (e.g. Borghini et al. 2016; Rogers and Grütter 2009; Schmädicke et al. 2015). The abundance of Fe in the upper mantle rock-forming minerals such as olivine, pyroxene, and garnet can significantly influence their elasticity (e.g. Speziale et al. 2005). Indeed, the Fe effect on the elasticity of olivine, enstatite, and garnet at high *P*-*T* conditions is well-documented (e.g. Lu et al. 2013; Mao et al. 2015; Zhang and Bass 2016b). However, the influence of Fe substitution on the elasticity of diopside at high *P*-*T* conditions has yet to be addressed, even though Cpx is an abundant mineral in the upper mantle and knowing its single-crystal elasticity is crucial to understand the seismic structure and geodynamic processes of the upper mantle (Forte et al. 2002; Speziale et al. 2014). In addition, we should also note that the Cpx in the upper-mantle peridotite and pyroxenite contain not only Fe, but also some amount of Al (e.g. Ackerman et al. 2012; Borghini et al. 2016; Davis et al. 2009; El Atrassi et al. 2013; Gysi et al. 2011), which is also known to influence the elastic moduli of pyroxenes (e.g. Hao et al. 2019a; Kandelin and Weidner 1988b; Zhang and Bass 2016b).

In this study, we have measured the acoustic wave velocities (V_P and V_S) of single-crystal $Di_{80}Hd_{20}$ in a diamond anvil cell (DAC) up to ~18.5 GPa at room temperature by using BLS method coupled with single-crystal XRD, in order to determine the equation of state and crystallographic orientations of the diopside crystal platelets at high-pressure conditions and, thus, reliably derive the full set of single-crystal elastic moduli for $Di_{80}Hd_{20}$. These results were then used to evaluate the effects of high-pressure and Fe-Mg substitution on the single-crystal elasticity of Mg-rich Cpx in the Di-Hd series including the sound velocities, elastic moduli and velocity anisotropy as well as applied, together with previous studies and thermoelastic modelling, to decipher the cause for low-velocity anomalies atop the 410-km discontinuity.

EXPERIMENTS

Natural single-crystal diopside from an ultramafic rock located in Jiuzigou area, Feng County, Shanxi Province, China, was used in this study. Based on electron microprobe analysis (JEOL Hyperprobe JXA-8500F) using an accelerating voltage of 15 kV and a beam current of 10 nA, the chemical formula of our natural diopside is $Ca_{0.99}Mg_{0.79}Fe_{0.21}Si_{2.01}O_6$, which can be regarded as $Di_{80}Hd_{20}$ (Table S1). Analysis of the synchrotron XRD patterns of the crystals using an incident X-ray of 0.3344 Å at the GeoSoilEnviroConsortium for the Advanced Radiation Sources (GSECARS) of the Advanced Photon Source (APS), Argonne National Laboratory (ANL) showed a monoclinic structure with the lattice parameters a=9.778(3) Å, b=8.945(3) Å, c=5.258(2) Å, β=105.794(5)°, V=442.52(8) Å^3. Based on the results from EMPA and XRD measurements the density of the sample is 3.345(1) g/cm^3 at ambient conditions.

Monoclinic diopside has 13 independent single-crystal elastic moduli. We thus selected three pieces of single crystals that possessed nearly orthogonal crystallographic orientation for the BLS measurements (Fig. 1). As determined by single-crystal XRD at beamline 13-BMD of GSECARS, the crystallographic planes of the three pieces are P1 (-0.17, 0.26, 0.94), P2 (0.24, 0.96, -0.18) and P3 (0.92, -0.12, 0.24), which are close to (001), (010) and (100) orientations, respectively (Fig. 1). These sample pieces were prepared and polished with water as lubricant to platelets of 20-25 μm in thickness using a 3M diamond lapping films of 9 μm, 3 μm, 1 μm, and 0.3 μm successively. The thin polished platelets were then cleaved into several square pieces of desired size (~70×90 μm) to be loaded into a DAC for high-pressure measurements. A rhenium gasket was pre-indented to a thickness of 50-60 μm by a pair of diamond anvils of 500 μm culet size, and a hole of 320 μm in diameter was subsequently drilled in the pre-indented area and used as the sample chamber. Three single-crystal platelets were then placed into the sample chamber, together with a few ruby spheres of approximately 5 um in diameter as the pressure indicator (Mao et al. 1986). Neon gas was then loaded into the sample chamber and used as the pressure medium using the gas loading system located in the Mineral Physics Laboratory of the University of Texas at Austin (Fan et al. 2019a; Mao et al. 2015).

High-pressure BLS combined with XRD measurements were also performed at beamline 13-BMD of APS. An incident X-ray beam of 0.3344 Å wavelength focused to ~3×7 μm^2 area (Sinogeikin et al. 2006) was used to determine the unit-cell volume of the crystal in the DAC. Pressures were determined from the ruby fluorescence spectra (Mao et al. 1986), while pressure uncertainties were calculated using multiple measurements before and after the collection of the BLS spectra for each pressure point. To ensure the pressure stability of the experiments, we stabilized the sample chamber at least 30 minutes for each given pressure point, and continuously monitored the pressure using the ruby fluorescence spectra until the pressure was sufficiently stable for the BLS experiments. Analysis of the XRD patterns of the sample was used to determine the unit cell volumes and thus density of $Di_{80}Hd_{20}$ at each pressure before and after the BLS measurements. The Brillouin system was equipped with a Coherent Verdi V2 solid-state laser with a wavelength of 532 nm, a Perkin Elmer MP983 photocounting module with a low dark count rate of <2 counts/s at room temperature (Sinogeikin et al. 2006), and a JRS six-pass Sandercock-type piezoelectrically scanning tandem Fabry-Pérot interferometer (Sandercock 1982). BLS spectra were collected in the symmetric forward scattering geometry with an external scattering angle of 50° (Fan et al. 2019b), which was calibrated using the elastic moduli of standard silicate glass (Corning 7980), distilled water, and single-crystal MgO (Ostwald et al. 1977; Sinogeikin and Bass 2000; Zhang et al. 2011). The laser beam focal spot on the sample position was approximately 15 μm in diameter. The acoustic V_P and V_S velocities of the sample were derived from the analysis of the Brillouin frequency shift as follows:

$$V_{P,S} = \frac{\lambda_0 \Delta v_B}{2\sin\frac{\theta}{2}} \quad (1)$$

where $V_{P,S}$ is the acoustic compressional or shear wave velocity, λ_0 is the incident laser wavelength, Δv_B is the Brillouin frequency shift, and θ is the external scattering angle.

RESULTS

High-pressure BLS spectra of the single-crystal $Di_{80}Hd_{20}$ as well as XRD spectra were collected up to ~18.5 GPa at room temperature (Fig. 1). The measured Brillouin frequency shifts of the crystal platelets were converted to velocities using equation (1). Most of the BLS spectra showed strong V_P and two polarized V_S peaks with high signal-to-noise ratios except for some crystallographic directions where the V_P or V_S peaks were weakly observable due to the intrinsic anisotropy of the elasto-optic coupling in monoclinic diopside (Nelson et al. 1972). Brillouin signals of the neon pressure medium were also observed at pressures below ~8 GPa, but they were too weak to be seen in the BLS spectra when the pressure was above 8 GPa. For each

This is a preprint, the final version is subject to change, of the American Mineralogist (MSA)
Cite as Authors (Year) Title. American Mineralogist, in press.
DOI: https://doi.org/10.2138/am-2020-7075

platelet at each given pressure, BLS spectra were collected in 19 different crystallographic directions from 0 to 180° of the azimuthal angle at an interval of 10° (Fig. 2). The measured V_P and V_S vary significantly as a function of the azimuthal angle, indicating strong elastic anisotropy of our sample at high pressures. Furthermore, both V_P and V_S of $Di_{80}Hd_{20}$ increase with increasing pressure.

Single-crystal elastic moduli of $Di_{80}Hd_{20}$ at each given pressure (Tables S2 and S3) were evaluated by the best-fit to the measured acoustic velocities at various crystallographic directions along the planes using the Christoffel's equation (Every 1980):

$$\left|C_{ijkl}n_j n_l - \rho V_{P,S}{}^2\delta_{ik}\right| = 0 \quad (2)$$

where n_j and n_l are the direction cosines of the phonon wave vector, ρ is the density at each pressure, δ_{ik} is the Kronecker delta function, C_{ijkl} is the elastic stiffness tensor in full suffix notation. However, in the following we will use the Voigt notation, C_{ij}, in which $_i$ represents the stress component and $_j$ is for the strain component. The detailed relationship between tensor and contracted quantities in Voigt notation is given elsewhere (Duffy 2018; Nye 1985). The calculated acoustic velocities from the best-fit elastic model are in excellent agreement with the experimental velocities at high pressures (Fig. 2). The root-mean-square deviation (RMS) for the fitting is about 35-50 m/s, which is <1% of the measured velocities. Nine of the 13 independent single-crystal elastic moduli (longitudinal (C_{11}, C_{22}, C_{33}), shear (C_{44}, C_{55}, C_{66}), and off-diagonal (C_{12}, C_{13}, C_{23})) of $Di_{80}Hd_{20}$ increase smoothly with increasing pressure, while the other off-diagonal elastic moduli (C_{15}, C_{25}, C_{35}, and C_{46}) decrease almost linearly with increasing pressure (Fig. 3 and Table S3). Furthermore, the three off-diagonal elastic moduli (C_{15}, C_{25}, and C_{46}) are much smaller than the rest of the off-diagonal moduli, especially at high pressures. The best-fit values of C_{25} and C_{46} are even slightly negative at high pressures, this phenomenon is similar to previous study of Di_{100} (Sang and Bass 2014).

Using the derived single-crystal elastic moduli of $Di_{80}Hd_{20}$, the adiabatic bulk and shear moduli at ambient conditions and high pressures were calculated according to the Voigt-Reuss-Hill averages (Fig. 4a and Tables S2-S3) (Hill 1952). The derived adiabatic bulk (K_{S0}) and shear moduli (G_0) of $Di_{80}Hd_{20}$ at ambient conditions are 117(2) and 70(1) GPa, respectively. Compared with the results of Di_{100} (Sang et al. 2011) at ambient conditions, the substitution of 20 mol.% Fe in diopside increases K_{S0} by ~1.7% (~2 GPa) but reduces G_0 by ~4.1% (~3 GPa). In addition, the K_S of $Di_{80}Hd_{20}$ is indistinguishable from that of Di_{100} at high pressure, but its G is lower than that of Di_{100} by ~4 GPa (Fig. 4a). The pressure derivatives of the elastic moduli at 300 K (Table S4 and Table 1) were obtained by fitting the moduli at high pressure using the third- or fourth-order Eulerian strain equation (Birch 1978). The first- and second-pressure derivatives of K_S and G were derived to be $(\partial K_S/\partial P)_T$=5.0(2), $(\partial^2 K_S/\partial P^2)_T$=-0.12(4) (GPa^{-1}), and $(\partial G/\partial P)_T$=1.72(9), $(\partial^2 G/\partial P^2)_T$=-0.05(2) (GPa^{-1}), respectively.

The aggregate compressional (V_P) and shear (V_S) wave velocities of $Di_{80}Hd_{20}$ were calculated using the equations:

$$V_P = \sqrt{\frac{K_S + \frac{4G}{3}}{\rho}} \quad (3)$$

$$V_S = \sqrt{\frac{G}{\rho}} \quad (4)$$

The aggregate velocities of $Di_{80}Hd_{20}$ at ambient conditions are V_P=7.92(1) km/s and V_S=4.57(1) km/s, which are ~1.7% and ~3.2% lower than that of Di_{100}, respectively (Table S2). However, both V_P and V_S of $Di_{80}Hd_{20}$ at high pressures are lower than those of Di_{100} by ~0.18 km/s in the entire pressure range (Fig. 4b).

DISCUSSION

Fe effects on the single-crystal elasticity of diopside

Combining BLS and single-crystal XRD measurements, we have determined the single-crystal elasticity of $Di_{80}Hd_{20}$ at ambient and high-pressure conditions (Figs. 3-4 and Tables S2-S3). Table S2 and Figure 5 compare single-crystal elastic moduli results at ambient conditions obtained in the present study for $Di_{80}Hd_{20}$ and previous studies for end-member diopside and hedenbergite using BLS method (Kandelin and Weidner 1988a; Levien et al. 1979; Sang et al. 2011) (Fig. 5).

The single-crystal elastic moduli of nearly end-member diopside at ambient condition have been measured by Levien et al. (1979) and Sang et al. (2011) using BLS method. Although these two studies have almost identical experimental sample compositions ($Di_{98}Hd_1Jd_1$ vs $Di_{97}Hd_2Jd_1$) and most of C_{ij}s and K_S between these two studies agree well with each other within uncertainties, other moduli (C_{22}, C_{66}, C_{13}, C_{15}, and G) show a large difference (~ 6-12 GPa). The exact reasons for these discrepancies are unknown (Sang et al. 2011). However, considering the improvements of BLS technique in the recent decades that has now higher signal-to-noise ratio and count rate (Bass and Zhang 2015; Li et al. 2019; Speziale et al. 2014; Wei et al. 2019), we chose the single-crystal elastic moduli data of Sang et al. (2011) for our comparison. On the other hand, there is just one set of single-crystal elastic moduli data available for end-member hedenbergite (Kandelin and Weidner 1988a).

Single-crystal elastic moduli (C_{ij}s)

As shown in Figure 5, comparison between our results of $Di_{80}Hd_{20}$ and previous results on diopside and hedenbergite end-members (Sang et al. 2011; Kandelin and Weidner 1988a) suggests a nearly linear trend between the single-crystal elastic moduli (C_{ij}s) and composition. Most of the independent single-crystal elastic moduli (C_{11}, C_{22}, C_{44}, C_{55}, C_{66}, C_{12}, C_{35}, and C_{46}) decrease smoothly with increasing hedenbergite content in the Di-Hd join, while other moduli (C_{33}, C_{13}, C_{23}, C_{15}, and C_{25}) increase linearly with increasing hedenbergite content (Fig. 5). This is consistent with a previous work on the diopside-jadeite join, which also shows systematic correlations between the composition and most of C_{ij} values (Hao et al. 2019a; Sang et al. 2011).

Aggregate elastic moduli and velocities (K_S, G, V_P, and V_S)

The aggregate elastic moduli (K_S and G) and velocities (V_P and V_S) of the Di-Hd join at ambient conditions also show that the substitution of hedenbergite in Di-Hd join has a linear effect on K_S, G, V_P, and V_S. Within experimental uncertainties, K_S linearly increases with Hd content, while G, V_P, and V_S decrease linearly with increasing Hd content (Fig. 6):

$$K_S = 114.5(6)+6.1(1.1)X_{Hd} \quad (7)$$

$$G = 72.4(2)-10.7(5)X_{Hd} \quad (8)$$

$$V_P = 8.04(1)-0.59(2)X_{Hd} \quad (9)$$

$$V_S = 4.71(1)-0.60(2)X_{Hd} \quad (10)$$

where $X_{Hd}=M_{Hd}/(M_{Di}+M_{Hd})$, X_{Hd} is the mole fraction, and M_{Di} and M_{Hd} are the molar content of diopside and hedenbergite along the Di-Hd join.

The pressure derivatives of elastic moduli (C_{ij}s, K_S, and G)

For a more thorough comparison with our results, we refitted the pressure derivatives of elastic moduli (C_{ij}s, K_S, and G) for Di_{100} by the third- or fourth-order Eulerian strain equation using the BLS data from Sang and Bass (2014) (Table S4 and Table 1). Comparative analysis of the results for Di_{100} (Sang and Bass, 2014) and $Di_{80}Hd_{20}$ (Table S4) shows that addition of Fe does not produce a visible effect on most of the pressure derivatives of C_{ij}s of diopside, although increasing the Fe content in diopside appears to have a weak negative effect on the pressure derivatives of C_{66}, C_{15}, and C_{46}. We have also compared the pressure derivatives of K_S and G for $Di_{80}Hd_{20}$ to the literature results (Table 1). The derived pressure derivatives of K_S and G for $Di_{80}Hd_{20}$ in this study are indistinguishable from the values of Di_{100} in previous BLS studies within experimental uncertainties (Sang and Bass, 2014). Additionally, the pressure derivatives of K_S and G in this study are also in good agreement with most of the values from previous UI and theoretical studies within uncertainties

(Table 1), except a distinct larger pressure derivative of K_S (6.2) and smaller pressure derivative of G (1.2) reported by theoretical studies (Matsui and Busing, 1984; Walker, 2012). Finally, all of the aforementioned comparisons seem to support the conclusion that the Fe content has a nearly linear effect on the elastic moduli (C_{ij}s, K_S, and G) but has a negligible effect on their pressure derivatives. Nevertheless, further evaluation of the relationship between the elastic moduli and Fe content at high-pressure conditions in the Di-Hd join will still require additional experimental data in the future, such as the single-crystal elasticity of hedenbergite at high pressures.

Fe effects on the velocity anisotropy of diopside

The velocity anisotropy together with the LPOs (lattice preferred orientations) of minerals are the key geophysical parameters for interpreting the observed seismic anisotropy within the upper mantle (e.g. Mainprice 2015; Wen et al. 2018). To understand the pressure effect on the velocity anisotropy of $Di_{80}Hd_{20}$, the V_P and V_S velocities at different propagation directions and anisotropy distributions were calculated using our derived C_{ij}s and density at each given pressure point (Mainprice 1990; Mainprice et al. 2000). The percentage anisotropy for V_P (AV_P) is defined here as:

$$AV_P = (V_{P,max}-V_{P,min}) /(V_{P,max}+V_{P,min}) \times 200\ \% \quad (5)$$

where $V_{P,max}$ and $V_{P,min}$ represent the maximum and minimum V_P velocities, respectively. The polarization anisotropy factor of V_S (AV_S), also called the shear wave-splitting factor, is the anisotropy percentage of the two V_S in a given direction. It is defined as:

$$AV_S = (V_{S1}-V_{S2}) /(V_{S1}+V_{S2}) \times 200\ \% \quad (6)$$

where V_{S1} and V_{S2} are the two orthogonally polarized shear wave velocities in the given propagation direction.

DOI: https://doi.org/10.2138/am-2020-7075

The contoured upper hemisphere stereograms of V_P and AV_S for $Di_{80}Hd_{20}$ at two representative pressure conditions shown in Figure 7 indicate that $Di_{80}Hd_{20}$ has high acoustic velocity anisotropy at ambient conditions, with the AV_P of 25.90% and AV_S of 21.22%. Compared to Di_{100} (Sang et al. 2011; Sang and Bass 2014), the addition of 20 mol.% Fe reduces the AV_P and AV_S by ~2.6 % and ~7.2 %, respectively at ambient conditions (Fig. 8). At elevated high-pressure conditions, these anisotropy factors notably decrease with increasing pressure. The AV_P and AV_S still have small-moderate but well resolvable values even at the maximum experimental pressure conditions (Figs. 7 and 8). For $Di_{80}Hd_{20}$, the AV_P is 14.10% and the AV_S is 15.74% at 18.5 GPa (Fig. 7). In addition, $Di_{80}Hd_{20}$ has a roughly similar AV_P to that of Di_{100} but a considerably lower AV_S than that of Di_{100} at high pressures (Fig. 8).

Fe effects on the sound velocities of diopside in the upper mantle

To better understand the influence of Fe on the acoustic velocity behavior of diopside, we have used our high-pressure elasticity results to model the velocity profiles of $Di_{80}Hd_{20}$ along an expected geotherm for normal mantle (Katsura et al. 2010) and a representative geotherm for cold subducted slab (Eberle et al. 2002) (Fig. 9). Although we did not measure the elastic moduli of $Di_{80}Hd_{20}$ at high temperatures in this study, Isaak et al. (2006) evaluated the effect of temperature on the elastic moduli of (Fe, Cr)-bearing diopside ($Di_{93}Hd_3Ur_2X_2$, where Ur is the molar fraction of ureyite (chrome-diopside) and X represent all of the other minor components). The measured temperature derivatives of the aggregate elastic moduli by Isaak et al. (2006) are indistinguishable with those values of Li and Neuville (2010) for Fe-free diopside within reciprocal uncertainties (Table 1). Assuming that the compositional (such as Fe) effect on the temperature derivatives of elastic moduli is negligible, we thus used the results of Isaak et al. (2006) to evaluate the temperature effect on the velocities of $Di_{80}Hd_{20}$ at upper mantle *P*-*T* conditions, and the thermoelastic parameters of upper mantle minerals utilized in our modeling are given in Table S5. In our modeling, we have neglected the coupling effect of high pressure and high temperature on K_S and

This is a preprint, the final version is subject to change, of the American Mineralogist (MSA)
Cite as Authors (Year) Title. American Mineralogist, in press.
DOI: https://doi.org/10.2138/am-2020-7075

G. K_S and *G* under ambient pressure and high temperature are then derived using their temperature derivatives. We then used the fourth-order Birch-Murnaghan Equation of State (EoS) (Birch 1978) to calculate the finite strain at given pressure and corresponding high temperature. The fourth-order Eulerian finite-strain equations (Birch 1978) are then used to derive the corresponding K_S and *G* for each mineral. After calculating the aggregate K_S and *G* using the Voigt-Ruess-Hill averages (Hill 1952), we can then calculate the V_P and V_S at high pressure and temperature.

Our modeling was limited to the upper-mantle region ranging from 200 km to 400 km depth because of the much more complex mineralogical, geochemical, and seismic heterogeneities above 200 km depth (Jordan 1975; Grand and Helmberger, 1984). The modeled velocity profiles show that the substitution of Fe in diopside can significantly decrease the V_P and V_S at upper mantle conditions (Fig. 9). Compared to Di_{100}, the V_P and V_S of $Di_{80}Hd_{20}$ are reduced by ~1.8% and ~3.5%, respectively along both the expected normal mantle geotherm and the representative cold subducted slab geotherm. Furthermore, the V_P and V_S profiles of $Di_{80}Hd_{20}$ are also ~3.3-5.7% and ~3.1-6.6% lower than the velocity profiles of AK135 model, respectively at 400 km depth (Fig. 9).

IMPLICATION

Since the first observation of the LVZ atop the 410-km discontinuity in 1990s (Revenaugh and Sipkin 1994), this seismic structure has been observed in both global and regional studies including subduction zones and continental cratons (e.g. Schaeffer and Bostock 2010; Tauzin et al. 2010; Vinnik and Farra 2007; Wang et al. 2018). Most of the observed LVZs are interpreted to be of the compositional origin (e.g. Speziale et al. 2005; Tauzin et al. 2017). As an abundant upper mantle mineral, the presence and abundance pyroxene (Cpx and Opx) in the upper mantle may be responsible for the LVZ atop the 410-km discontinuity because the relative proportions of constituent minerals change significantly over the relevant upper mantle depths (e.g. McDonough and Rudnick 1998).

Previous studies have suggested that Opx and Cpx would become unstable at ~300 km to transition zone depth under normal mantle geotherm conditions, because they are dissolved into garnet (Frost 2008; Ringwood 1982). However, pyroxenes could survive at greater depths in the cold subducted slabs because the pyroxene-garnet transition could be inhibited at relatively low subducted slab temperatures (Bina 2013; Lazarz et al. 2019; Nishi et al. 2013; van Mierlo et al. 2013; Xu et al. 2019). Although the abundance of Cpx and Opx are around 15 vol.% and 10 vol.%, respectively, in the pyrolite model mantle composition (Ringwood 1991), there is also evidence for local enrichments of pyroxene in the upper mantle, such as mantle-derived pyroxenite xenoliths (e.g. Lambart et al. 2013; Yang et al. 2016). Furthermore, a recent study has shown that most of pyroxenes in the cold subducted slab geotherm would promote slab stagnation atop 410 km depth if they are metastably preserved in significant quantities (e.g. Xu et al. 2017). Thus, pyroxenite (including Fe-enriched pyroxenite) could exist atop 410 km depth at the cold subducted slab conditions.

To evaluate the potential influence of pyroxene (Cpx and Opx) on the seismic feature of LVZ atop the 410-km discontinuity, we have calculated the velocity profiles (V_P and V_S) of pyroxenite at upper mantle 300-400 km depth range along a cold subudcted slab geotherm. According to the mineral compositions of representative pyroxenites in the upper mantle (e.g. Ackerman et al. 2012; Aulbach and Jacob 2016; Borghini et al. 2016; Dantas et al. 2007; Gysi et al. 2011; Henry et al. 2017; Kopylova et al. 1999; Lambart et al. 2013; Tilhac et al. 2017; Varas-Reus et al. 2018; Yang et al. 2016; Zhang et al. 2016), the pyroxenite model in our modelling contains ~60 vol.% Cpx, ~30 vol.% Opx and ~10 vol.% olivine.

Previous studies have proposed that pyroxenite could have a relatively low X_{Mg} value between 0.75 and 0.85, with an average value of 0.8 (e.g. Borghini et al. 2016; Müller et al. 2013; Rogers and Grütter 2009; Tecchiato et al. 2018). Taking the effect of Fe content into account, we also assumed that X_{Mg}=0.8 for olivine, X_{Mg}=0.8 for Opx and X_{Mg}=0.8 for Cpx in our pyroxenite velocity modeling. The elasticity of

Fe-enriched olivine (~20 mol.% Fe) and Fe-enriched Opx (~20 mol.% Fe) were calculated using the linear relationship between Fe content and elasticity of olivine and Opx (Jackson et al. 2003, 2007; Mao et al. 2015; Wang et al. 2019; Webb and Jackson 1993; Zha et al. 1996; Zhang and Bass, 2016a, 2016b). In addition, Cpx in upper-mantle pyroxenite also contains approximately 5 mol.% Al (e.g. Ackerman et al. 2012; Davis et al. 2009; El Atrassi et al. 2013; Gysi et al. 2011), which is considered in our velocity modeling. The modeled velocity profiles of Fe-enriched pyroxenite are also compared with the AK135 seismic model (Kennett et al. 1995) (Fig. 10). Our results show that the V_P and V_S profiles of pyroxenite are ~3.2% and ~2.5% lower than AK135 model at 400 km depth, respectively (Fig. 10). These corresponding V_P and V_S reductions of Fe-enriched pyroxenite are consistent with the seismic observations of LVZ atop the 410-km discontinuity (e.g. Li et al. 2014; Song et al. 2004; Tauzin et al. 2010; Vinnik et al. 2010) (Fig. 11).

Additionally, previous studies also indicated that Fe-bearing pyroxenes containing resolvable amounts of H_2O can display enhanced electrical conductivity and contribute significantly to the bulk electrical conductivity of upper mantle in electromagnetic observations (e.g. Wang et al. 1999; Yang et al. 2011; Yang and McCammon 2012; Zhao and Yoshino 2016). That is, the observed high conductivity anomalies in some regions of the upper mantle can be explained by the presence of small amounts of hydrated pyroxene without invoking the presence of partial melt at these depths (e.g. Wang et al. 2008; Yang and McCammon 2012). Accordingly, it is conceivable that the presence of pyroxenite with enhanced Fe content and perhaps with a small amount of water may be the cause of low-velocity anomalies in the cold subducted slabs atop the 410-km discontinuity. We should emphasize that the aforementioned scenario is only applicable to the cold subducted slabs where the metastable pyroxene (Cpx and Opx) can be preserved even below 660-km discontinuity. On the contrary, due to the instability of pyroxene, other causes such as the existence of partial melting (Song et al. 2004; Vinnik et al. 2010) or thermal anomalies (Morishige et al. 2010; Obayashi et al. 2016), may play a more dominant role for the low-velocity anomalies atop the 410-km discontinuity in the normal upper mantle regions.

Acknowledgments

We acknowledge B. Li for the BLS experiments assistance, W. G. Zhou for his constructive suggestions and discussions. D. W. Fan acknowledges financial support from National Natural Science Foundation of China (41772043), Joint Research Fund in Huge Scientific Equipment (U1632112) under the cooperative agreement between NSFC and CAS, CAS "Light of West China" Program (Dawei Fan, 2017), Youth Innovation Promotion Association CAS (Dawei Fan, 2018434), and Innovation and Entrepreneurship Funding of High-Level Overseas Talents of Guizhou Province (Dawei Fan, [2019]10). J. F. Lin acknowledges support from Geophysics and CSEDI Programs of the U.S. National Science Foundation. J. G. Xu acknowledges financial support from National Natural Science Foundation of China (41802043), and CAS "Light of West China" Program (Jingui Xu, 2019). This work was performed at GeoSoilEnviroCARS (The University of Chicago, Sector 13), Advanced Photon Source (APS), Argonne National Laboratory. GeoSoilEnviroCARS is supported by the National Science Foundation (EAR-0622171) and the Department of Energy (DE-FG02-94ER14466) under Contract No. DE-AC02-06CH11357. This research used resources at the Advanced Photon Source, a U.S. Department of Energy (DOE) Office of Science User Facility operated for the DOE Office of Science by Argonne National Laboratory under Contract No. DE-AC02-06CH11357. Readers can access the additional data in the supporting information.

References

Ackerman, L., Špaček, P., Medaris, G., Hegner, E., Svojtka, M., and Ulrych, J. (2012) Geochemistry and petrology of pyroxenite xenoliths from Cenozoic alkaline basalts, Bohemian Massif. Journal of Geosciences, 57, 199-219.

Akaogi, M., Yano, M., Tejima, Y., Iijima, M., and Kojitani, H. (2004) High-pressure transitions of diopside and wollastonite: Phase equilibria and thermochemistry of $CaMgSi_2O_6$, $CaSiO_3$ and $CaSi_2O_5$-$CaTiSiO_5$ system. Physics of the Earth and Planetary Interiors, 143-144, 145-156.

Aulbach, S., and Jacob, D.E. (2016) Major- and trace-elements in cratonic mantle eclogites and pyroxenites reveal heterogeneous sources and metamorphic processing of low-pressure protoliths. Lithos, 262, 586-605.

Azough, F., and Freer, R. (2000) Iron diffusion in single-crystal diopside. Physics and Chemistry of Minerals, 27(10), 732-740.

Bass, J.D. Sinogeikin, S.V., and Li, B.S. (2008) Elastic properties of minerals: a key for understanding the composition and temperature of Earth's interior. Elements, 4(3), 165-170.

Bass, J.D., and Zhang, J.S. (2015) Theory and practice: techniques for measuring high-P–T elasticity. In: Schubert, G. (eds.), Treatise on Geophysics, 2nd edition, vol 2, pp. 293-312, Oxford: Elsevier.

Bina, C.R. (2013) Mineralogy: Garnet goes hungry. Nature Geoscience, 6(5), 335-336.

Bina, C.R., Stein, S., Marton, F.C., and Van Ark, E.M. (2001). Implications of slab mineralogy for subduction dynamics. Physics of the Earth and Planetary Interiors, 127(1-4), 51-66.

Birch, F. (1978) Finite strain isotherm and velocities for single-crystal and polycrystalline NaCl at high pressure and 300 K. Journal of Geophysical Research, 83(B3), 1257-1268.

Borghini, G., Rampone, E., Zanetti, A., Class, C., Cipriani, A., Hofmann, A.W., and Goldstein, S.L. (2016) Pyroxenite layers in the northern Apennines' upper mantle (Italy)-generation by pyroxenite melting and melt infiltration. Journal of Petrology, 57(4), 625-653.

Collins, M.D., and Brown, J.M. (1998) Elasticity of an upper mantle clinopyroxene. Physics and Chemistry of Minerals, 26(1), 7-13.

Dantas, C., Ceuleneer, G., Gregoire, M., Python, M., Freydier, R., Warren, J., and Dick, H.J.B. (2007) Pyroxenites from the Southwest Indian Ridge, 9-16ºE: Cumulates from Incremental

Melt Fractions Produced at the Top of a Cold Melting Regime. Journal of Petrology, 48(4), 647-660.

Davis, F.A., Tangeman, J.A., Tenner, T.J., and Hirschmann, M.M. (2009) The composition of KLB-1 peridotite. American Mineralogist, 94(1), 176-180.

Duffy, T.S. (2018) Single-crystal elastic properties of minerals and related materials with cubic symmetry. American Mineralogist, 103(6), 977-988.

Duffy, T.S., and Ahrens, T.J. (1992) Sound velocities at high pressure and temperature and their geophysical implications. Journal of Geophysical Research, 97(B4), 4503-4520.

Duffy, T.S., and Anderson, D.L. (1989) Seismic velocities in mantle minerals and the mineralogy of the upper mantle. Journal of Geophysical Research, 94(B2), 1895-1912.

Eberle, M.A., Grasset, O., and Sotin, C. (2002) A numerical study of the interaction between the mantle wedge, subducting slab, and overriding plate. Physics of the Earth and Planetary Interiors, 134(3-4), 191-202.

El Atrassi, F., Brunet, F., Chazot, G., Bouybaouène, M., and Chopin, C. (2013) Metamorphic and magmatic overprint of garnet pyroxenites from the Beni Bousera massif (northern Morocco): Petrography, mineral chemistry and thermobarometry. Lithos, 179, 231-248.

Every, A. (1980) General closed-form expressions for acoustic waves in elastically anisotropic solids. Physical Review B, 22(4), 1746-1760.

Fan, D.W., Fu, S.Y., Yang, J., Tkachev, S.N., Prakapenka, V.B., and Lin, J.F. (2019a) Elasticity of single-crystal periclase at high pressure and temperature: the effect of iron on the elasticity and seismic parameters of ferropericlase in the lower mantle. American Mineralogist, 104(2), 262-275.

Fan, D.W., Xu, J.G., Lu, C., Tkachev, S.N., Li, B., Ye, Z.L., Huang, S.J., Prakapenka, V.B., and Zhou, W.G. (2019b) Elasticity of single-crystal low water-content hydrous pyrope at high pressure and high temperature conditions. American Mineralogist, 104(7), 1022-1031

This is a preprint, the final version is subject to change, of the American Mineralogist (MSA)
Cite as Authors (Year) Title. American Mineralogist, in press.
DOI: https://doi.org/10.2138/am-2020-7075

Fan, D.W., Mao, Z., Yang, J., and Lin, J.F. (2015) Determination of the full elastic tensor of single crystals using shear wave velocities by Brillouin spectroscopy. American Mineralogist, 100(11-12), 2590-2601.

Finger, L.W., and Ohashi, Y. (1976) The thermal expansion of diopside to 800 °C and a refinement of the crystal structure at 700 °C. American Mineralogist, 61, 303-310.

Forte, A.M., Mitrovica, J.X., and Espesset, A. (2002) Geodynamic and seismic constraints on the thermochemical structure and dynamics of convection in the deep mantle. Philosophical Transactions of the Royal Society A, 360(1800), 2521-2543.

Frost, D.J. (2008) The upper mantle and transition zone. Elements, 4, 171-176.

Fukao, Y., and Obayashi, M. (2013) Subducted slabs stagnant above, penetrating through, and trapped below the 660 km discontinuity. Journal of Geophysical Research, 118(11), 5920-5938.

Fumagalli, P., and Klemme, S. (2015) Mineralogy of the Earth: phase transitions and mineralogy of the upper mantle. In: Schubert, G. (eds.) Treatise on Geophysics, 2nd edition, vol 2, pp. 7-31, Oxford, Elsevier.

Grand, S.P., and Helmberger, D.V. (1984) Upper mantle shear structure of North America. Geophysical Journal International, 76(2), 399-438.

Gysi, A.P., Jagoutz, O., Schmidt, M.W., and Targuisti, K. (2011) Petrogenesis of Pyroxenites and Melt Infiltrations in the Ultramafic Complex of Beni Bousera, Northern Morocco. Journal of Petrology, 52(9), 1679-1735.

Hao, M., Pierotti, C., Tkachev, S., Prakapenka, V., and Zhang, J.S. (2019a) The single-crystal elastic properties of the jadeite-diopside solid solution and their implications for the composition dependent seismic properties of eclogite. American Mineralogist, 104, 1016-1021

Hao, M., Zhang, J.S., Pierotti, C.E., Ren, Z., and Zhang, D.Z. (2019b) High-pressure single-crystal elasticity and thermal equation of state of omphacite and their implications for the seismic properties of eclogite in the Earth's interior. Journal of Geophysical Research, 124, 2368- 2377.

Henry, H., Tilhac, R., Griffin, W.L., O'Reilly, S.Y., Satsukawa, T., Kaczmarek, M.A., Grégoire, M., and Ceuleneer, G. (2017) Deformation of mantle pyroxenites provides clues to geodynamic processes in subduction zones: Case study of the Cabo Ortegal Complex, Spain. Earth and Planetary Science Letters, 472, 174-185.

Hill, R. (1952) The elastic behaviour of a crystalline aggregate. Proceedings of the Physical Society-Section A, 65(5), 349-354.

Hu, Y., Kiefer, B., Bina, C.R., Zhang, D.Z., and Dera, P. (2017) High-Pressure γ-$CaMgSi_2O_6$: Does penta-coordinated silicon exist in the Earth's mantle? Geophysical Research Letters, 44(22), 11340-11348.

Irifune, T., Miyashita, M., Inoue, T., Ando, J., Funakoshi, K., and Utsumi, W. (2000) High-pressure phase transformation in $CaMgSi_2O_6$ and implications for origin of ultra-deep diamond inclusions. Geophysical Research Letters, 27(21), 3541-3544.

Isaak, D.G., and Ohno, I. (2003) Elastic constants of chrome-diopside: application of resonant ultrasound spectroscopy to monoclinic single-crystals. Physics and Chemistry of Minerals, 30(7), 430-439.

Isaak, D.G., Ohno, I., and Lee, P.C. (2006) The elastic constants of monoclinic single-crystal chrome-diopside to 1300 K. Physics and Chemistry of Minerals, 32(10), 691-699.

Jackson, J.M., Palko, J.W., Andrault, D., Sinogeikin, S.V., Lakshtanov, D.L., Wang, J.Y., Bass, J.D., and Zha, C.S. (2003) Thermal expansion of natural orthoenstatite to 1473 K. European Journal of Mineralogy, 15(3), 469-473.

Jackson, J.M., Sinogeikin, S.V., and Bass, J.D. (2007) Sound velocities and single-crystal elasticity of orthoenstatite to 1073 K at ambient pressure. Physics of the Earth and Planetary Interiors, 161(1-2), 1-12.

Jordan, T.H. (1975) Lateral heterogeneity and mantle dynamics. Nature, 257(5529), 745-750.

Kandelin, J., and Weidner, D.J. (1988a) Elastic properties of hedenbergite. Journal of Geophysical Research, 93(B2), 1063-1072.

Kandelin, J., and Weidner, D.J. (1988b) The single-crystal elastic properties of jadeite. Physics of the Earth and Planetary Interiors, 50, 251-260.

Katsura, T., Yoneda, A., Yamazaki, D., Yoshino, T., and Ito, E. (2010) Adiabatic temperature profile in the mantle. Physics of the Earth and Planetary Interiors, 183(1-2), 212-218.

Kennett, B.L.N., Engdahl, E.R., and Buland, R. (1995) Constraints on seismic velocities in the Earth from traveltimes. Geophysical Journal International, 122(1), 108-124.

Kim, Y.-H., Ming, L.C., and Manghnani, M.H. (1994) High-pressure phase transformations in a natural crystalline diopside and a synthetic $CaMgSi_2O_6$ glass. Physics of the Earth and Planetary Interiors, 83(1), 67-79.

Kopylova, M.G., Russell, J.K., and Cookenboo, H. (1999) Petrology of Peridotite and Pyroxenite Xenoliths from the Jericho Kimberlite: Implications for the Thermal State of the Mantle beneath the Slave Craton, Northern Canada. Journal of Petrology, 40(1), 79-104.

Lambart, S., Laporte, D., and Schiano, P. (2013) Markers of the pyroxenite contribution in the major-element compositions of oceanic basalts: Review of the experimental constraints. Lithos, 160-161, 14-36.

Lazarz, J.D., Dera, P., Hu, Y., Meng, Y., Bina, C.R., and Jacobsen, S.D. (2019) High-pressure phase transitions of clinoenstatite. American Mineralogist, 104(6), 897-904.

Lee, C.-T.A. (2003) Compositional variation of density and seismic velocities in natural peridotites at STP conditions: Implications for seismic imaging of compositional heterogeneities in the upper mantle. Journal of Geophysical Research, 108(B9), 2441.

Levien, L., and Prewitt, C.T. (1981) High-pressure structural study of diopside. American Mineralogist, 66(3-4), 315-323.

Levien, L., Weidner, D.J., and Prewitt, C.T. (1979) Elasticity of diopside. Physics and Chemistry of Minerals, 4(2), 105-113.

Li, B.S., and Neuville, D.R. (2010) Elasticity of diopside to 8 GPa and 1073 K and implications for the upper mantle. Physics of the Earth and Planetary Interiors, 183(3-4), 398-403.

Li, G.H., Sui, Y., and Zhou, Y.Z. (2014) Low-velocity layer atop the mantle transition zone in the lower Yangtze Craton from P waveform triplication. Chinese Journal of Geophysics (in chinese), 57(7), 2362-2371.

Li, X.Y., Shi, W.G., Liu, X.D., and Mao, Z. (2019) High-pressure phase stability and elasticity of ammonia hydrate. American Mineralogist, 104(9), 1307-1314

Liebermann, R.C., and Mayson, D.J. (1976) Elastic properties of polycrystalline diopside ($CaMgSi_2O_6$). Physics of the Earth and Planetary Interiors, 11(3), P1-P4.

Lu, C., Mao, Z., Lin, J.F., Zhuravlev, K.K., Tkachev, S.N., and Prakapenka, V.B. (2013) Elasticity of single-crystal iron-bearing pyrope up to 20 GPa and 750 K. Earth and Planetary Science Letters, 361, 134-142.

Luth, R.W., and Canil, D. (1993) Ferric iron in mantle-derived pyroxenes and a new oxybarometer for the mantle. Contributions to Mineralogy and Petrology, 113(2), 236-248.

Mainprice, D. (1990) A Fortran Program to Calculate Seismic Anisotropy from the Lattice Preferred Orientation of Minerals. Computers & Geosciences, 16(3), 385-393.

Mainprice, D. (2015) Seismic Anisotropy of the Deep Earth from a Mineral and Rock Physics Perspective. In: Schubert, G. (eds.), Treatise on Geophysics, 2nd edition, vol 2, pp. 487-538, Oxford: Elsevier.

Mainprice, D., Barruol, G., and Ben Ismail, W. (2000) The anisotropy of the Earth's mantle: From single crystal to polycrystal. In: Karato, S.I., Stixrude, L., Liebermann, R., Masters, G., and Forte, A. (eds.), Mineral Physics and Seismic Tomography from the Atomic to the Global Scale, Geophysical Monograph Series, vol. 177, pp. 237-264, American Geophysical Union, Washington, DC.

Mainprice, D., Tommasi, A., Couvy, H., Cordier, P., and Frost, D.J. (2005) Pressure sensitivity of olivine slip systems: Implicaitons for the interpretation of seismic anisotropy of the Earth's upper mantle. Nature, 433(7027), 731-733.

Mao, H.K., Xu, J., and Bell, P.M. (1986) Calibration of the ruby pressure gauge to 800 kbar under quasi-hydrostatic conditions. Journal of Geophysical Research, 91(B5), 4673-4676.

Mao, Z., Fan, D.W., Lin, J.F., Yang, J., Tkachev, S.N., Zhuravlev, K., and Prakapenka, V.B. (2015). Elasticity of single-crystal olivine at high pressures and temperatures. Earth and Planetary Science Letters, 426, 204-215.

Matsui, M., and Busing, W.R. (1984) Calculation of the elastic constants and high-pressure properties of diopside, $CaMgSi_2O_6$. American Mineralogist, 69(11), 1090-1095.

McDonough, W.F., and Rudnick, R.L. (1998) Mineralogy and composition of the upper mantle. Reviews in Mineralogy and Geochemistry, 37(1), 139-164.

Morishige, M., Honda, S., and Yoshida, M. (2010) Possibility of hot anomaly in the sub-slab mantle as an origin of low seismic velocity anomaly under the subducting Pacific plate. Physics of the Earth and Planetary Interiors, 183(1-2), 353-365.

Müller, T., Dohmen, R., Becker, H.W., ter Heege, J.H., and Chakraborty, H.S. (2013) Fe-Mg interdiffusion rates in clinopyroxene: experimental data and implications for Fe-Mg exchange geothermometers. Contributions to Mineralogy and Petrology, 166(6), 1563-1576.

Nelson, D.F., Lazay, P.D., and Lax, M. (1972) Brillouin scattering in anisotropic media: calcite. Physical Review B, 6(8), 3109-3120.

Nishi, M., Kubo, T., Ohfuji, H., Kato, T., Nishihara, Y., and Irifune, T. (2013) Slow Si-Al interdiffusion in garnet and stagnation of subducting slabs. Earth and Planetary Science Letters, 361, 44-49.

Nye, J.F. (1985) Physical Properties of Crystals: Their Representation by Tensors and Matrices. Oxford University Press, Oxford, UK.

Obayashi, M., Sugioka, H., Yoshimitsu, J., and Fukao, Y. (2006) High temperature anomalies oceanward of subducting slabs at the 410-km discontinuity. Earth and Planetary Science Letters, 243(1-2), 149-158.

Oguri, K., Funamori, N., Sakai, F., Kondo, T., Uchida, T., and Yagi, T. (1997) High-pressure and high-temperature phase relations in diopside $CaMgSi_2O_6$. Physics of the Earth and Planetary Interiors, 104(4), 363-370.

Ostwald, J., Pazold, W., and Weis, O. (1977) High-resolution Brillouin spectroscopy of water. Applied Physics, 13(4), 351-356.

Putirka, K., Ryerson, F.J., Perfit, M., and Ridley, W.I. (2011) Mineralogy and composition of the Oceanic mantle. Journal of Petrology, 52(2), 279-313.

Revenaugh, J., and Sipkin, S. (1994) Seismic evidence for silicate melt atop the 410-km mantle discontinuity. Nature, 369(6480), 474-476.

Richwood, P.C., Mathias, M., and Siebert, J.C. (1968) A study of garnets from eclogite and peridotite xenoliths found in kimberlite. Contributions to Mineralogy and Petrology, 19(4), 271-301.

Ringwood, A.E. (1982) Phase transformations and differentiation in subducted lithosphere: implications for mantle dynamics, basalt petrogenesis, and crustal evolution. The Journal of Geology, 90(6), 611-643.

Ringwood, A.E. (1991) Phase transformations and their bearing on the constitution and dynamics of the mantle. Geochimica et Cosmochimica Acta, 55(8), 2083-2110.

Rogers, A., and Grütter, H.S. (2009) Fe-rich and Na-rich megacryst clinopyroxene and garnet from the Luxinga kimberlite cluster, Lunda Sul, Angola. Lithos, 112(S2), 942-950.

Sandercock, J.R. (1982) Trends in Brillouin scattering: studies of opaque materials, supported films, and central modes. In: Cardona, M., and Guntherodt, J. (eds.), Topics in Applied Physics, pp. 173-206, Springer-Verlag, Berlino.

Sang, L.Q., and Bass, J.D. (2014) Single-crystal elasticity of diopside to 14 GPa by Brillouin scattering. Physics of the Earth and Planetary Interiors, 228, 75-79.

Sang, L.Q., Vanpeteghem, C.B., Sinogeikin, S.V., and Bass, J.D. (2011) The elastic properties of diopside, $CaMgSi_2O_6$. American Mineralogist, 96(1), 224-227.

Schaeffer, A.J., and Bostock, M.G. (2010) A low-velocity zone atop the transition zone in northwestern Canada. Journal of Geophysical Research, 115, B06302.

Schmädicke, E., Will, T.M., and Mezger, K. (2015) Garnet pyroxenite from the Shackleton Range, Antarctica: Intrusion of plume-derived picritic melts in the continental lithosphere during Rodinia breakup? Lithos, 238, 185-206.

Sinogeikin, S.V., and Bass, J.D. (2000) Single-crystal elasticity of pyrope and MgO to 20 GPa by Brillouin scattering in the diamond cell. Physics of the Earth and Planetary Interiors, 120(1-2), 43-62.

Sinogeikin, S.V., Bass, J.D., Prakapenka, V., Lakshtanov, D., Shen, G., Sanchez-Valle, C., and Rivers, M. (2006) Brillouin spectrometer interfaced with synchrotron radiation for simultaneous X-ray density and acoustic velocity measurements. Review of Scientific Instruments, 77(10), 103905.

Song, T.-R.A., Helmberger, D.V., and Grand, S.P. (2004) Low-velocity zone atop the 410-km seismic discontinuity in the northwestern United States. Nature, 427(6974), 530-533.

Spetsius, Z.V., Taylor, L.A., Valley, J.W., Deangelis, M.T., Spicuzza, M., Ivanov, A.S., and Banzeruk, V.I. (2008) Diamondiferous xenoliths from crustal subduction: garnet oxygen isotopes from the Nyurbinskaya pipe, Yakutia. European Journal of Mineralogy, 20(3), 375-385.

Speziale, S., Jiang, F., and Duffy, T.S. (2005) Compositional dependence of the elastic wave velocities of mantle minerals: Implications for seismic properties of mantle rocks. In: van der Hilst, R., Bass, J.D., Matas, J., and Trampert, J. (eds.), Earth's Deep Mantle: Structure, Composition, and Evolution, pp. 301-320, American Geophysical Union, Washington, DC.

Speziale, S. Marquardt, H., and Duffy, T.S. (2014) Brillouin scattering and its application in geosciences. Reviews in Mineralogy & Geochemistry, 78(1), 543-603.

Stixrude, L., and Lithgow-Bertelloni, C. (2005) Mineralogy and elasticity of the oceanic upper mantle: origin of the low-velocity zone. Journal of Geophysical Research, 110(B3), B03204.

Takazawa, E., Frey, F.A., Shimizu, N., and Obata, M. (2000) Whole rock compositional variations in an upper mantle peridotite (Horoman, Hokkaido, Japan): are they consistent with a partial melting process? Geochimica et Cosmochimica Acta, 64(4), 695-716.

Tauzin, B., Debayle, E., and Wittlinger, G. (2010) Seismic evidence for a global low-velocity layer within the Earth's upper mantle. Nature Geoscience, 3(10), 718-721.

Tauzin, B., Kim, S., and Kennett, B.L.N. (2017) Pervasive seismic low-velocity zones within stagnant plates in the mantle transition zone: Thermal or compositional origin? Earth and Planetary Science Letters, 477, 1-13.

Tauzin, B., van der Hilst, R.D., Wittlinger, G., and Ricard, Y. (2013) Multiple transition zone seismic discontinuities and low velocity layers below western United States. Journal of Geophysical Research, 118(5), 2307-2322.

Tecchiato, V., Gaeta, M., Mollo, S., Bachmann, O., von Quadt, A., and Scarlato, P. (2018) Snapshots of primitive arc magma evolution recorded by clinopyroxene textural and compositional variations: The case of hybrid crystal-rich enclaves from Capo Marargiu Volcanic District (Sardinia, Italy). American Mineralogist, 103, 899-910.

Thompson, R.M., and Downs, R.T. (2008) The crystal structure of diopside at pressure to 10 GPa. American Mineralogist, 93(1), 177-186.

Tilhac, R., Grégoire, M., O'Reilly, S.Y., Griffin, W.L., Henry, H., and Ceuleneer, G. (2017) Sources and timing of pyroxenite formation in the sub-arc mantle: Case study of the Cabo Ortegal Complex, Spain. Earth and Planetary Science Letters, 474, 490-502.

Tribaudino, M., Prencipe, M., Bruno, M., and Levy, D. (2000) High-pressure behavior of Ca-rich C2/c clinopyroxenes along the join diopside-enstatite ($CaMgSi_2O_6$-$Mg_2Si_2O_6$). Physics and Chemistry of Minerals, 27(9), 656-664.

van Mierlo, W., Langenhorst, F., Frost, D., and Rubie, D. (2013) Stagnation of subducting slabs in the transition zone due to slow diffusion in majoritic garnet. Nature Geoscience, 6(5), 400-403.

Varas-Reus, M.I., Garrido, C.J., Marchesi, C., Bosch, D., and Hidas, K. (2018) Genesis of ultra-high pressure garnet pyroxenites in orogenic peridotites and its bearing on the compositional heterogeneity of the Earth's mantle. Geochimica et Cosmochimica Acta, 232, 303-328.

Vinnik, L., and Farra, V. (2007) Low S velocity atop the 410-km discontinuity and mantle plumes. Earth and Planetary Science Letters, 262(3-4), 398-412.

Vinnik, L., Ren, Y., Stutzmann, E., Farra, V., and Kiselev, S. (2010) Observations of S410p and S350p phases at seismograph stations in California. Journal of Geophysical Research, 115, B05303.

Walker, A.M. (2012) The effect of pressure on the elastic properties and seismic anisotropy of diopside and jadeite from atomic scale simulation. Physics of the Earth and Planetary Interiors, 192-193, 81-89.

Wang, D.J., Li, H.P., Yi, L., and Shi, B.Q. (2008) The electrical conductivity of upper-mantle rocks: water content in the upper mantle. Physics and Chemistry of Minerals, 35(3), 157-162.

Wang, S.H., Chen, T., Cai, N., Qi, X.T., Fiege, A., Liebermann, R.C., and Li, B.S. (2019) Pressure-induced velocity softening in natural orthopyroxene at mantle temperature. American Mineralogist, 104(8), 1173-1179.

Wang, X.J., Han, G.J., and Li, J. (2018) Low-velocity layer atop the upper mantle transition zone in Northwest Pacific subduction zone. Chinese Journal of Geophysics (in chinese), 61(3), 819-831.

Wang, Z.C., Ji, S.C., and Dresen, G. (1999) Hydrogen-enhanced electrical conductivity of diopside crystals. Geophysical Research Letters, 26(6), 799-802.

Webb, S.L., and Jackson, I. (1993) The pressure dependence of the elastic moduli of single-crystal orthopyroxene $(Mg_{0.8}Fe_{0.2})SiO_3$. European Journal of Mineralogy, 5, 1111-1119.

Wei, W., Li, X., Sun, N., Tkachev, S.N., and Mao, Z. (2019) Sound velocity of Neon at high pressures and temperatures by Brillouin scattering. American Mineralogist, https://doi.10.2138/am-2019-7033.

Wen, D.P., Wang, Y.F., Zhang, J.F., and Jin, Z.M. (2018) Anisotropic growth of olivine during crystallization in basalts from Hawaii: Implications for olivine fabric development. American Mineralogist, 103(5), 735-741.

Woodland, A.B. (2009) Ferric iron contents of clinopyroxene from cratonic mantle and partitioning behaviour with garnet. Lithos, 112(S2), 1143-1149.

Xu, J.G, Zhang, D.Z, Dera, P., Zhang, B., and Fan, D.W. (2017) Experimental evidence for the survival of augite to transition zone depths, and implications for subduction zone dynamics. American Mineralogist, 102(7), 1516-1524.

Xu, J.G., Zhang, D.Z., Fan, D.W., Dera, P., Shi, F., and Zhou, W.G. (2019) Thermoelastic properties of eclogitic ternary garnets and omphacites: Implications for deep subduction of oceanic crust and density anomalies in the upper mantle. Geophysical Research Letters, 46, 179-188.

Xu, J.G, Zhang, D.Z, Fan, D.W., Zhang, J.S., Hu, Y., Guo, X.Z., Dera, P., and Zhou, W.G. (2018) Phase transitions in orthoenstatite and subduction zone dynamics: effects of water and transition metal ions. Journal of Geophysical Research, 123(4), 2723-2737.

Yang, J., Tong, X.Y., Lin, J.F., Okuchi, T., and Tomioka, N. (2015) Elasticity of ferropericlase across the spin crossover in the Earth's lower mantle. Scientific Reports, 5, 17188.

Yang, X.Z., Keppler, H., McCammon, C., Ni, H.W., Xia, Q.K., and Fan, Q.C. (2011) Effect of water on the electrical conductivity of lower crustal clinopyroxene. Journal of Geophysical Research, 116, B04208.

Yang, X.Z., and McCammon, C. (2012) Fe^{3+}-rich augite and high electrical conductivity in the deep lithosphere. Geology, 40(2), 131-134.

Yang, Z.F., Li, J., Liang, W.F., and Luo, Z.H. (2016) On the chemical markers of pyroxenite contributions in continental basalts in Eastern China: Implications for source lithology and the origin of basalts. Earth-Science Reviews, 157, 18-31.

Yoshizawa, K., Miyake, K., and Yomogida, K. (2010) 3D upper mantle structure beneath Japan and its surrounding region from inter-station dispersion measurements of surface waves. Physics of the Earth and Planetary Interiors, 183(1-2), 4-19.

Zha, C.S., Duffy, T.S., Downs, R.T., Mao, H.K., and Hemley, R.J. (1996) Sound velocity and elasticity of single-crystal forsterite to 16 GPa. Journal of Geophysical Research, 101(B8), 17535-17545.

Zhang, J.S., and Bass, J.D. (2016a) Sound velocities of olivine at high pressures and temperatures and the composition of Earth's upper mantle. Geophysical Research Letters, 43(18), 9611-9618.

Zhang, J.S., and Bass, J.D. (2016b) Single-crystal elasticity of natural Fe-bearing orthoenstatite across a high-pressure phase transition. Geophysical Research Letters, 43(16), 8473-8481.

Zhang, J.S., Bass, J.D., Taniguchi, T., Goncharov, A.F., Chang, Y.Y., and Jacobsen, S.D. (2011) Elasticity of cubic boron nitride under ambient conditions, Journal of Applied Physics, 109, 063521.

Zhang, L., Ahsbahs, H., Hafner, S.S., and Kutoglu, A. (1997) Single-crystal compression and crystal structure of clinopyroxene up to 10 GPa. American Mineralogist, 82(3-4), 245-258.

Zhang, S.B., Zheng, Y.F., Zhao, Z.F., and Yuan, H.L. (2016) The extremely enriched mantle beneath the Yangtze Craton in the Neoproterozoic: Constraints from the Qichun pyroxenite. Precambrian Research, 276, 194-210.

Zhao, C.C., and Yoshino, T. (2016) Electrical conductivity of mantle clinopyroxene as a function of water content and its implication on electrical structure of uppermost mantle. Earth and Planetary Science Letters, 447, 1-9.

Zhao, Y.S., Von Dreele, R.B., Zhang, J.Z., and Weidner, D.J. (1998) Thermoelastic equation of state of monoclinic pyroxene: $CaMgSi_2O_6$ diopside. The Review of High Pressure Science and Technology, 7, 25-27.

Zou, F., Wu, Z.Q., Wang, W.Z., and Wentzcovitch, R.M. (2018) An extended semi-analytical approach for thermoelasticity of monoclinic crystals: application to diopside. Journal of Geophysical Research, 123(9), 7629-7643.

Figure Captions

Figure 1. Representative Brillouin spectra of single-crystal $Di_{80}Hd_{20}$ at 12.70 GPa. Open circles: experimental data; solid lines: fitted V_P and V_S peaks, respectively. The inset is a representative photo of the three crystal platelets in the sample chamber at 12.70 GPa and 300 K. (Color online)

Figure 2. V_P and V_S velocities of single-crystal $Di_{80}Hd_{20}$ as a function of the azimuthal angle measured from the three crystal planes at 12.70 GPa and 300 K. Open circles: experimental data; solid lines: fitting results. (Color online)

Figure 3. Single-crystal elastic moduli (C_{ij}s) of $Di_{80}Hd_{20}$ as a function of pressure. Black solid symbols represent our experimental data; open red symbols are the experimental data for Di_{100} from Sang and Bass (2014). Solid lines are the fitted results using the third- or fourth-order Eulerian finite-strain equation. (Color online)

Figure 4. Aggregate elastic moduli (K_S and G) and velocities (V_P and V_S) of $Di_{80}Hd_{20}$ as a function of pressure. Black solid symbols represent our experimental data; open red symbols are the experimental data for Di_{100} from Sang and Bass (2014). Solid lines are the fitted results using the fourth-order Eulerian finite-strain equation. (Color online)

Figure 5. The variation of single-crystal elastic moduli (C_{ij}s) with Hd content in the diopside-hedenbergite system at ambient conditions. Solid symbols are derived from experimental Brillouin results for Di_{100} (Sang et al., 2011), $Di_{98}Hd_2$ (Sang et al., 2011), $Di_{80}Hd_{20}$ (This study) and Hd_{100} (Kandelin and Weidner, 1988a). Solid lines are linear fits to the Brillouin experimental data. (Color online)

DOI: https://doi.org/10.2138/am-2020-7075

Figure 6. The aggregate elastic moduli and velocities of Di-Hd as a function of the Hd content at ambient conditions. Solid symbols are derived from experimental Brillouin results for Di_{100} (Sang et al., 2011), $Di_{98}Hd_2$ (Sang et al., 2011), $Di_{80}Hd_{20}$ (This study) and Hd_{100} (Kandelin and Weidner, 1988a). Solid lines are linear fits to the Brillouin experimental data. (Color online)

Figure 7. Upper hemisphere pole figures of V_P and V_S splitting anisotropy of single-crystal $Di_{80}Hd_{20}$ at ambient conditions and 18.5 GPa. Calculations were performed using the petrophysical software UnicefCareware of Mainprice (1990) with the derived single-crystal elastic moduli and density from this study. (Color online)

Figure 8. Variation of V_P anisotropy and V_S splitting anisotropy factors (AV_P and AV_S) for single-crystal $Di_{80}Hd_{20}$ at high pressures. Black solid symbols represent our experimental data; open red symbols are the experimental data for Di_{100} from Sang and Bass (2014). (Color online)

Figure 9. Modeled V_P and V_S of Fe-enriched Cpx, Fe-free Cpx in the upper mantle along the expected normal mantle geotherm (a) (Katsura et al., 2010) and the representative subducted-slab geotherm (b) (Eberle et al., 2002). Red lines: $Di_{80}Hd_{20}$ (The parameters used to model V_P and V_S are from Finger and Ohashi 1976; Isaak et al. 2006; Hao et al. 2019a; This study); blue lines: Di_{100} (The parameters used to model V_P and V_S are from Finger and Ohashi 1976; Li and Neuville, 2010; Sang and Bass, 2014); dashed lines: AK135 (Kennett et al., 1995). Error bars represent the propagated uncertainties (±1σ). (Color online)

Figure 10. Modeled V_P and V_S of Fe-enriched pyroxenite model in the mid upper-mantle 300-400 km depth range along the representative subducted-slab geotherm (b) (Eberle et al., 2002). Red lines: Fe-enriched Pyroxenite, and dashed

lines: AK135 (Kennett et al., 1995). Error bars represent the propagated uncertainties (±1σ). (Color online)

Figure 11. Velocity difference (V_P (a) and V_S (b)) between petrological model with Fe-enriched pyroxenite along the cold subducted slab geotherm and AK135 at upper mantle 350-400 km range. The light blue region indicates the range of seismic velocity anomalies observed in the LVZ atop the MTZ at depths of 350-400 km. Red lines: velocity difference between Fe-enriched pyroxenite and AK135. (Color online)

Table 1 Bulk and shear moduli and their pressure and temperature derivatives of diopside at ambient conditions

References	Composition	Methods [a]	K_{S0} (GPa)	G_0 (GPa)	$(\partial K_S/\partial P)_T$	$(\partial^2 K_S/\partial P^2)_T$ (GPa^{-1})	$(\partial G/\partial P)_T$	$(\partial^2 G/\partial P^2)_T$ (GPa^{-1})	$(\partial K_S/\partial T)_P$ (GPa/K)	$(\partial^2 K_S/\partial T^2)_P$ (10^{-6}GPa/K^2)	$(\partial G/\partial T)_P$ (GPa/K)	$(\partial^2 G/\partial T^2)_P$ (10^{-6}GPa/K^2)
This study	$Di_{80}Hd_{20}$	BLS	116.6(8)	69.8(7)	5.0(2)	-0.12(4)	1.72(9)	-0.05(2)	—[b]	—[b]	—[b]	—[b]
Sang et al. (2011)	Di_{100}	BLS	114.6(7)	72.7(4)	—[b]	—[b]	—[b]	—[b]	—[b]	—[b]	—[b]	—[b]
Sang et al. (2011)	$Di_{97}Hd_2Jd_1$	BLS	113.7(8)	72.2(5)	—[b]	—[b]	—[b]	—[b]	—[b]	—[b]	—[b]	—[b]
Sang and Bass (2014)	Di_{100}	BLS	114.6(7)	72.7(4)	5.4(4)[d]	-0.2(1)[d]	1.9(2)[d]	-0.07(4)[d]	—[b]	—[b]	—[b]	—[b]
Levien et al. (1979)	$Di_{98}Hd_1Jd_1$	BLS	113[c]	67[c]	—[b]	—[b]	—[b]	—[b]	—[b]	—[b]	—[b]	—[b]
Kandelin and Weidner (1988)	Hd_{100}	BLS	120.4[c]	61.8[c]	—[b]	—[b]	—[b]	—[b]	—[b]	—[b]	—[b]	—[b]
Li and Neuville (2010)	Di_{100}	UI	116.4(7)	73.0(4)	4.9(1)	—[b]	1.6(1)	—[b]	-0.012(1)	—[b]	-0.011(1)	—[b]
Liebermann and Mayson (1976)	Di_{100}	UI	113[c]	75[c]	—[b]	—[b]	—[b]	—[b]	—[b]	—[b]	—[b]	—[b]
Isaak et al. (2003)	$Di_{93}Hd_3Ur_2X_2$	RUS	116.5(9)	72.8(4)	—[b]	—[b]	—[b]	—[b]	—[b]	—[b]	—[b]	—[b]
Isaak et al. (2006)	$Di_{93}Hd_3Ur_2X_2$	RUS	—[b]	—[b]	—[b]	—[b]	—[b]	—[b]	-0.0123[c]	—[b]	-0.00998[c]	—[b]
Walker (2012)	Di_{100}	DFT	122.6(6)	74.6(4)	4.7[c]	—[b]	1.2[c]	—[b]	—[b]	—[b]	—[b]	—[b]
Matsui and Busing (1984)	Di_{100}	CPP	105[c]	—[b]	6.2	—[b]	—[b]	—[b]	—[b]	—[b]	—[b]	—[b]
Zou et al. (2018)	Di_{100}	DFT	117.5[c]	71.8[c]	5.0[c]	-0.026[c]	1.56[c]	-0.0302[c]	-0.0150[c]	-1.66[c]	-0.00871[c]	-1.94[c]

Di: Diopside; Hd: Hedenbergite; Jd: Jadeite; Ur: Ureyite; X: unknown

[a] BLS: Brillouin Light Scattering; UI: Ultrasonic Interferometry; RUS: Resonant Ultrasound Spectroscopy; DFT: Density Functional Theory; CPP: classical pair potentials;

[b] The values are not available in the text.

[c] The uncertainties are not available in the text.

[d] Refitting by the fourth-order Eulerian finite-strain equation.

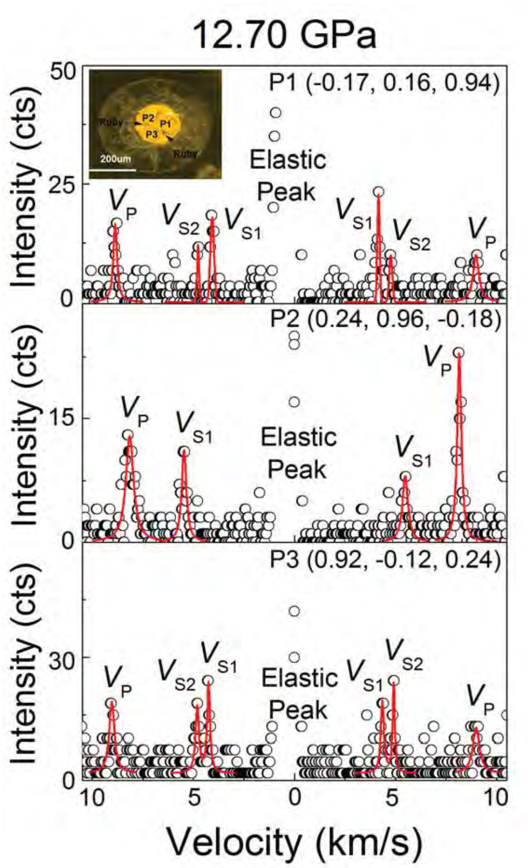
12.70 GPa
P1 (-0.17, 0.16, 0.94)
P2
P1
P3
Ruby
Ruby
200um
Elastic Peak
V_P
V_{S2}
V_{S1}
V_{S1}
V_{S2}
V_P
P2 (0.24, 0.96, -0.18)
V_P
V_{S1}
Elastic Peak
V_{S1}
V_P
P3 (0.92, -0.12, 0.24)
V_P
V_{S2}
V_{S1}
Elastic Peak
V_{S1}
V_{S2}
V_P
Intensity (cts)
50
25
0
15
0
30
0
10
5
0
5
10
Velocity (km/s)

Fig. 1

This is a preprint, the final version is subject to change, of the American Mineralogist (MSA)
Cite as Authors (Year) Title. American Mineralogist, in press.
DOI: https://doi.org/10.2138/am-2020-7075

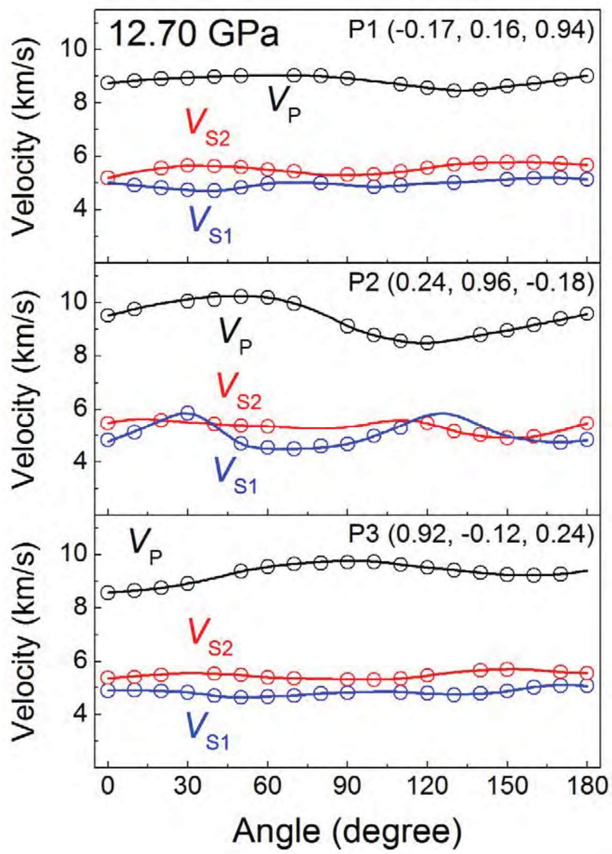

Fig. 2

This is a preprint, the final version is subject to change, of the American Mineralogist (MSA)
Cite as Authors (Year) Title. American Mineralogist, in press.
DOI: https://doi.org/10.2138/am-2020-7075

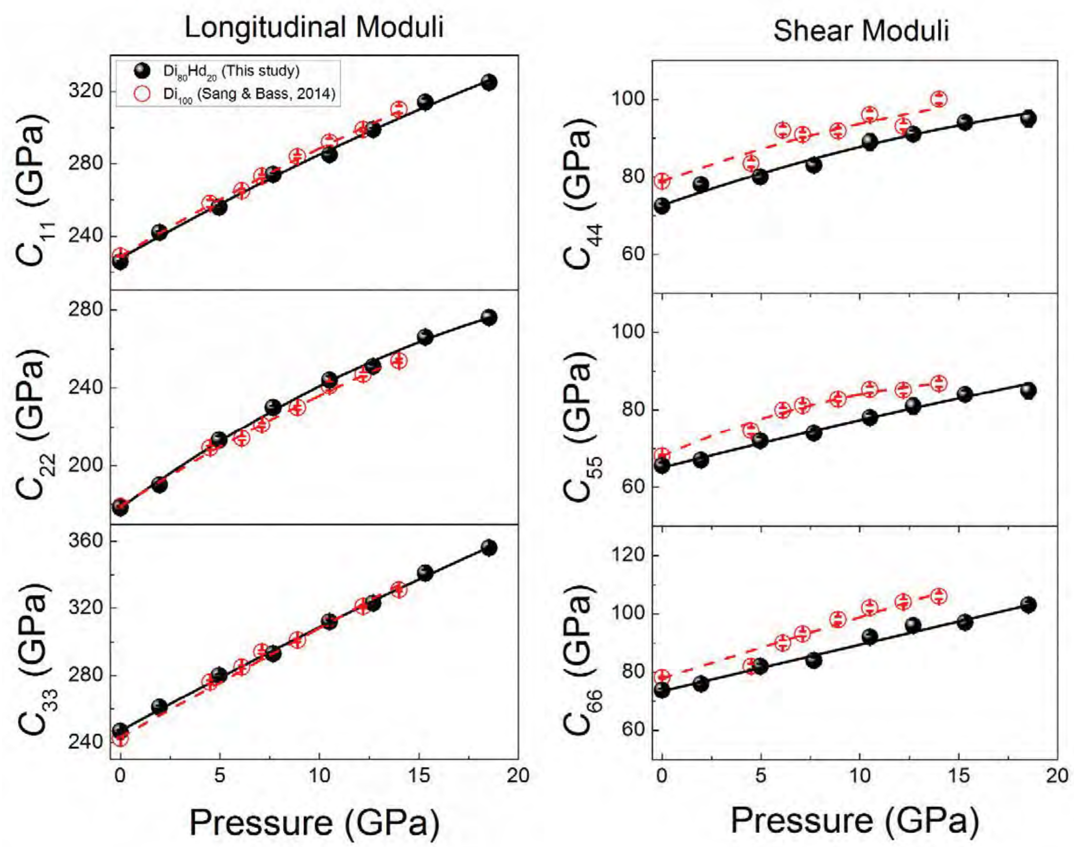

This is a preprint, the final version is subject to change, of the American Mineralogist (MSA)
Cite as Authors (Year) Title. American Mineralogist, in press.
DOI: https://doi.org/10.2138/am-2020-7075

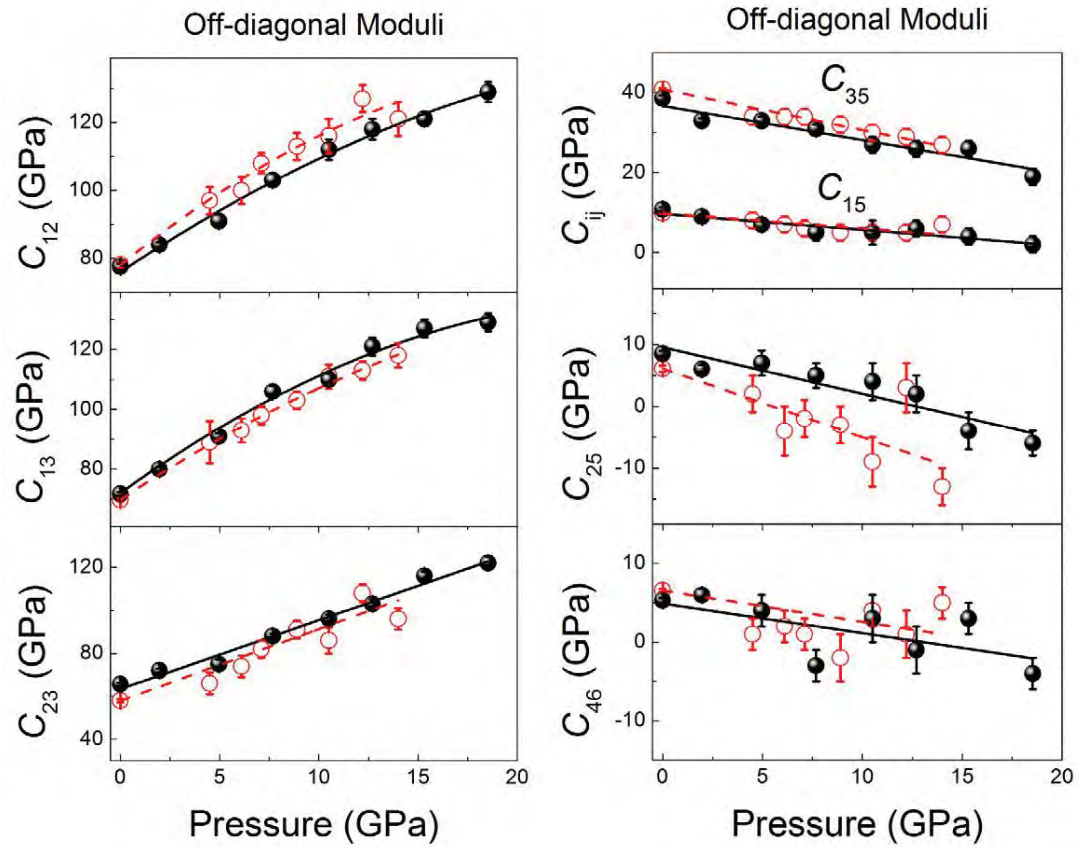

Fig. 3

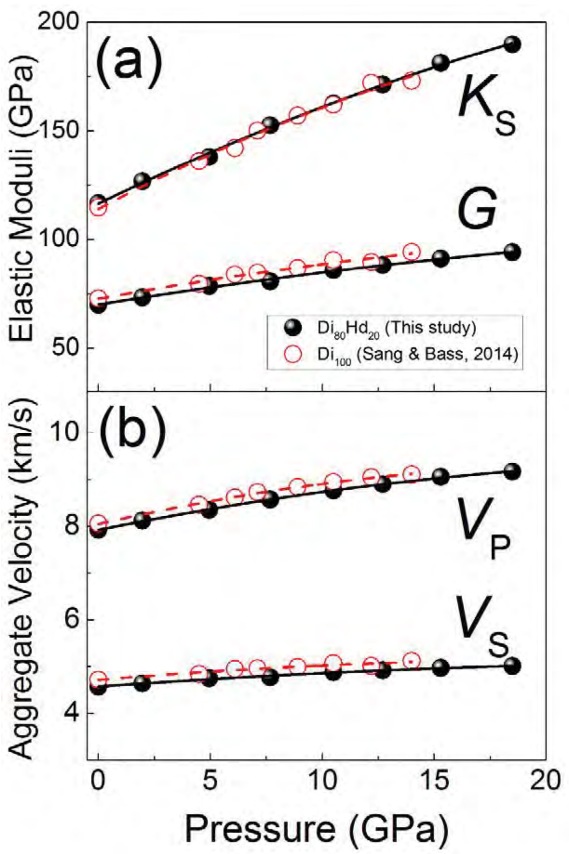
(a)
K_S
G
Elastic Moduli (GPa)
200
150
100
50
Di80Hd20 (This study)
Di100 (Sang & Bass, 2014)
(b)
V_P
V_S
Aggregate Velocity (km/s)
10
8
6
4
0
5
10
15
20
Pressure (GPa)

Fig. 4

DOI: https://doi.org/10.2138/am-2020-7075

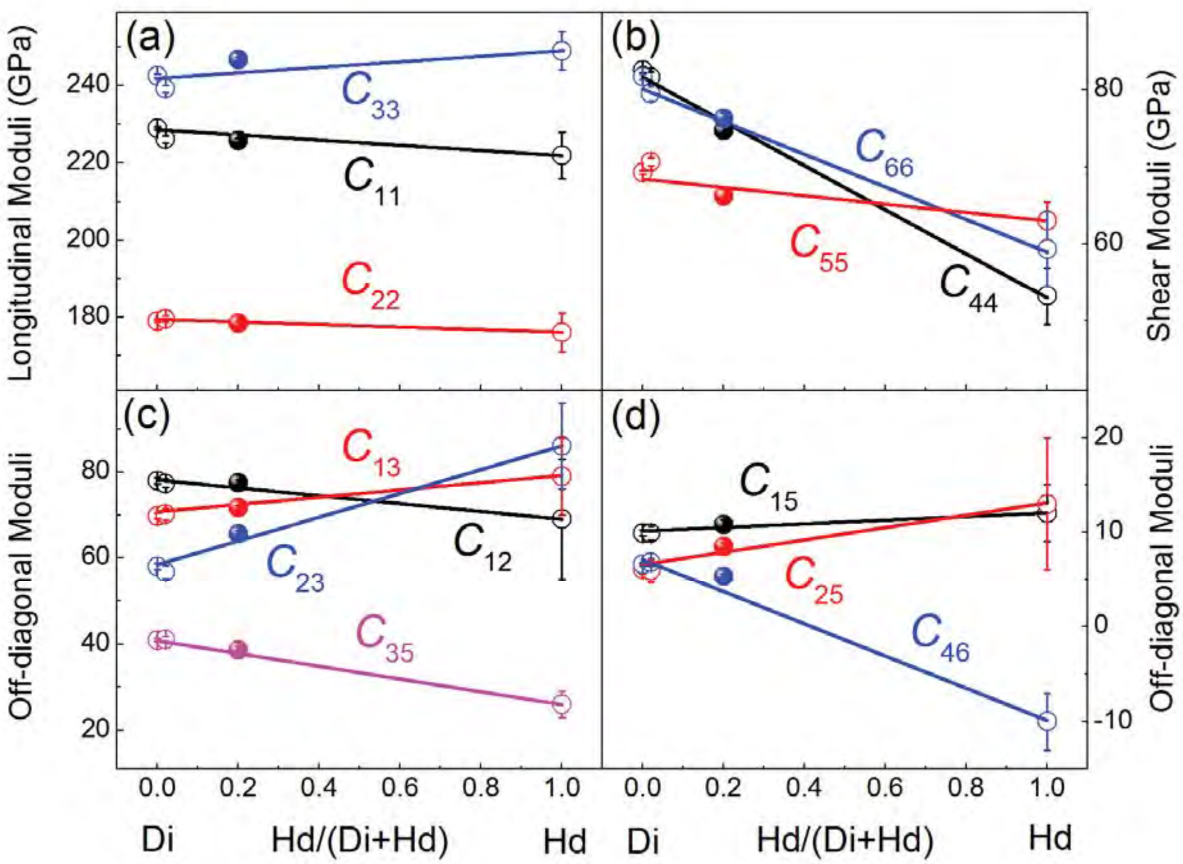

Fig. 5

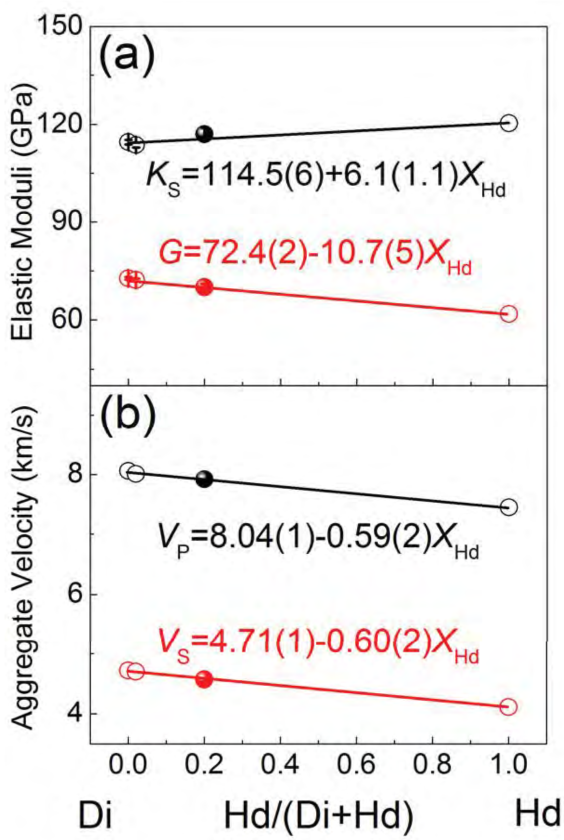
(a)
(b)
Elastic Moduli (GPa)
Aggregate Velocity (km/s)
K_S=114.5(6)+6.1(1.1)X_Hd
G=72.4(2)-10.7(5)X_Hd
V_P=8.04(1)-0.59(2)X_Hd
V_S=4.71(1)-0.60(2)X_Hd
150
120
90
60
8
6
4
0.0
0.2
0.4
0.6
0.8
1.0
Di
Hd/(Di+Hd)
Hd

Fig. 6

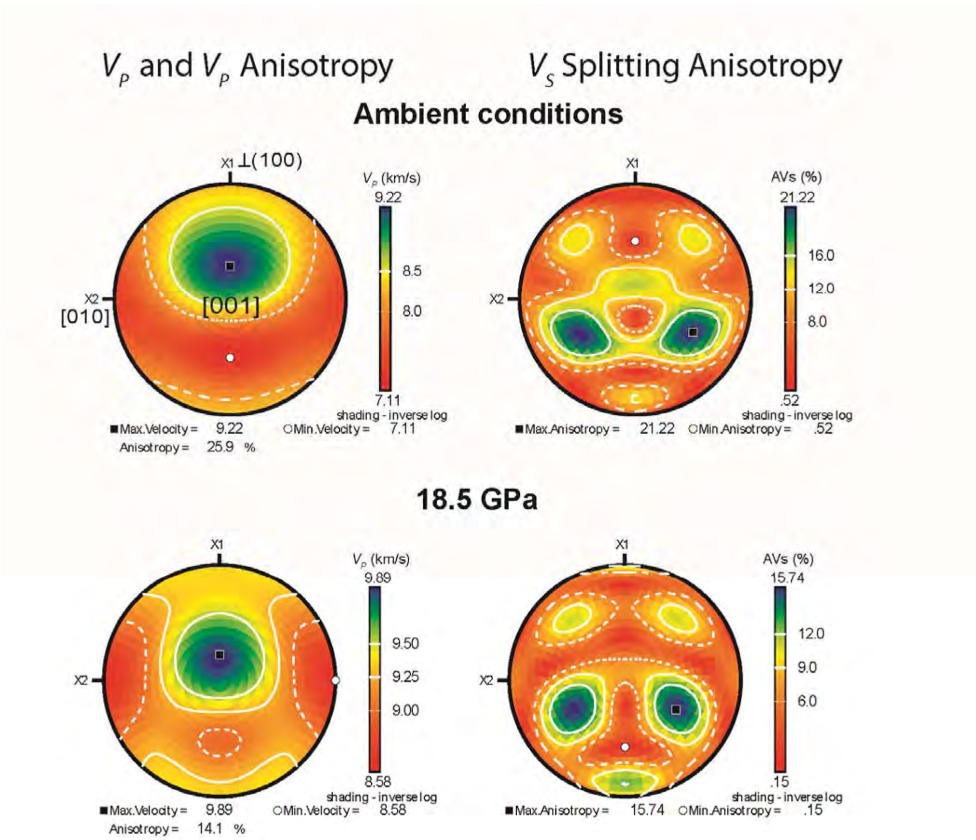

Vp and Vp Anisotropy
Vs Splitting Anisotropy
Ambient conditions
X1 ⊥(100)
X2
[010]
[001]
Vp (km/s)
9.22
8.5
8.0
7.11
shading - inverse log
■ Max.Velocity = 9.22
○ Min.Velocity = 7.11
Anisotropy = 25.9 %
X1
X2
AVs (%)
21.22
16.0
12.0
8.0
.52
shading - inverse log
■ Max.Anisotropy = 21.22
○ Min.Anisotropy = .52
18.5 GPa
X1
X2
Vp (km/s)
9.89
9.50
9.25
9.00
8.58
shading - inverse log
■ Max.Velocity = 9.89
○ Min.Velocity = 8.58
Anisotropy = 14.1 %
X1
X2
AVs (%)
15.74
12.0
9.0
6.0
.15
shading - inverse log
■ Max.Anisotropy = 15.74
○ Min.Anisotropy = .15

Fig. 7

This is a preprint, the final version is subject to change, of the American Mineralogist (MSA)
Cite as Authors (Year) Title. American Mineralogist, in press.
DOI: https://doi.org/10.2138/am-2020-7075

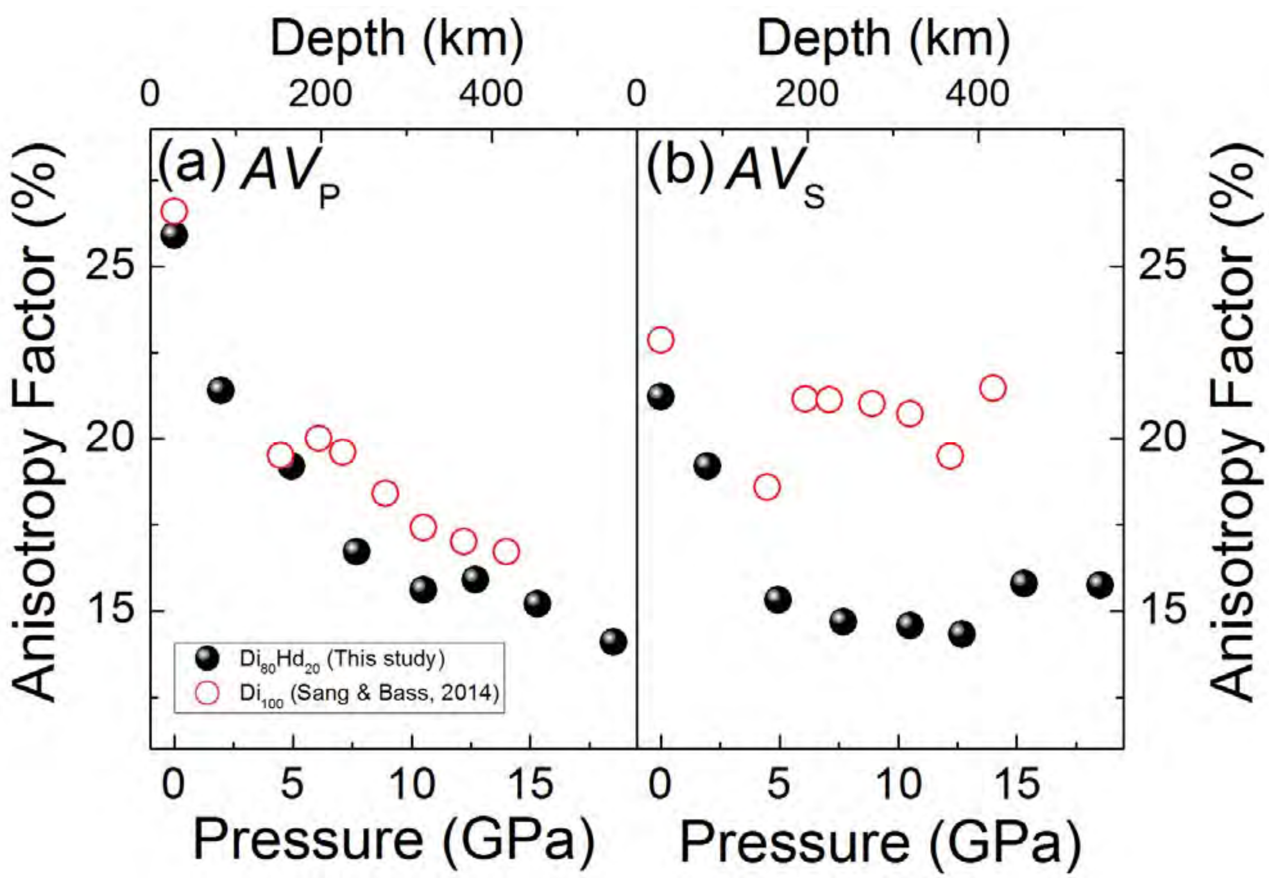

Fig. 8

This is a preprint, the final version is subject to change, of the American Mineralogist (MSA)
Cite as Authors (Year) Title. American Mineralogist, in press.
DOI: https://doi.org/10.2138/am-2020-7075

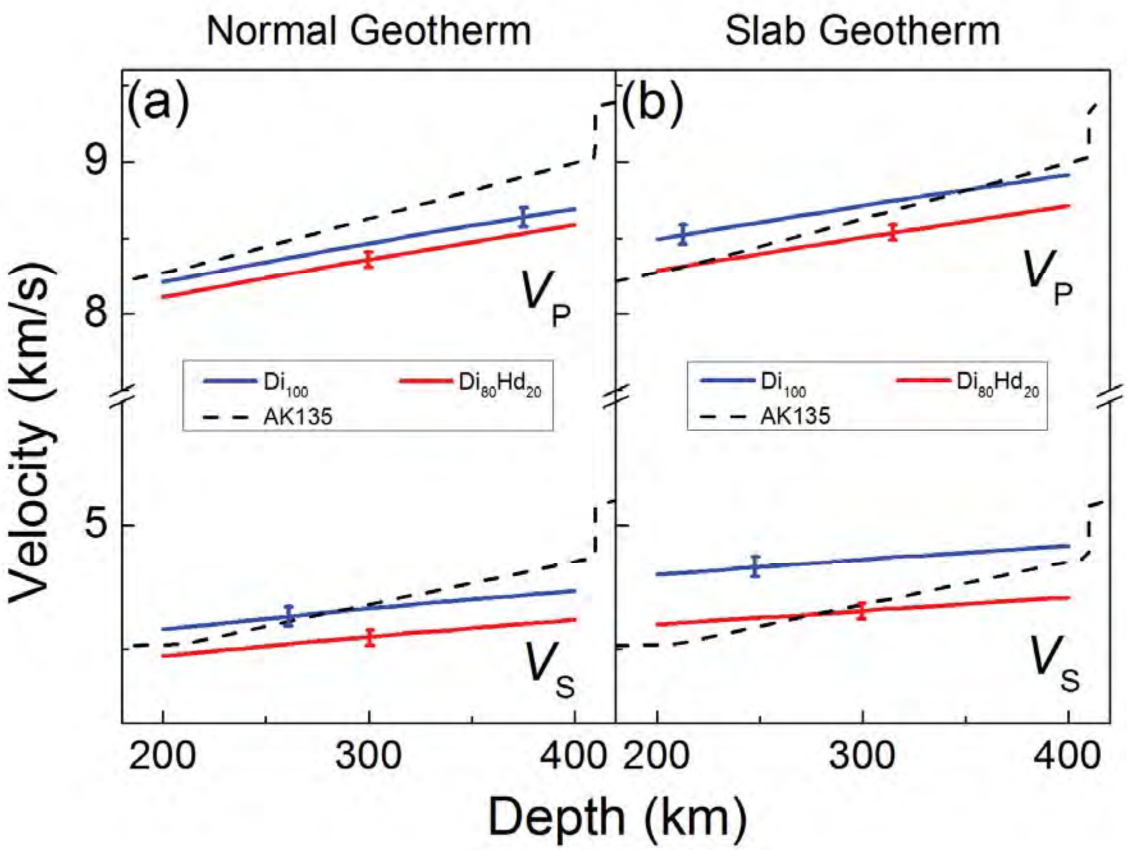

Fig. 9

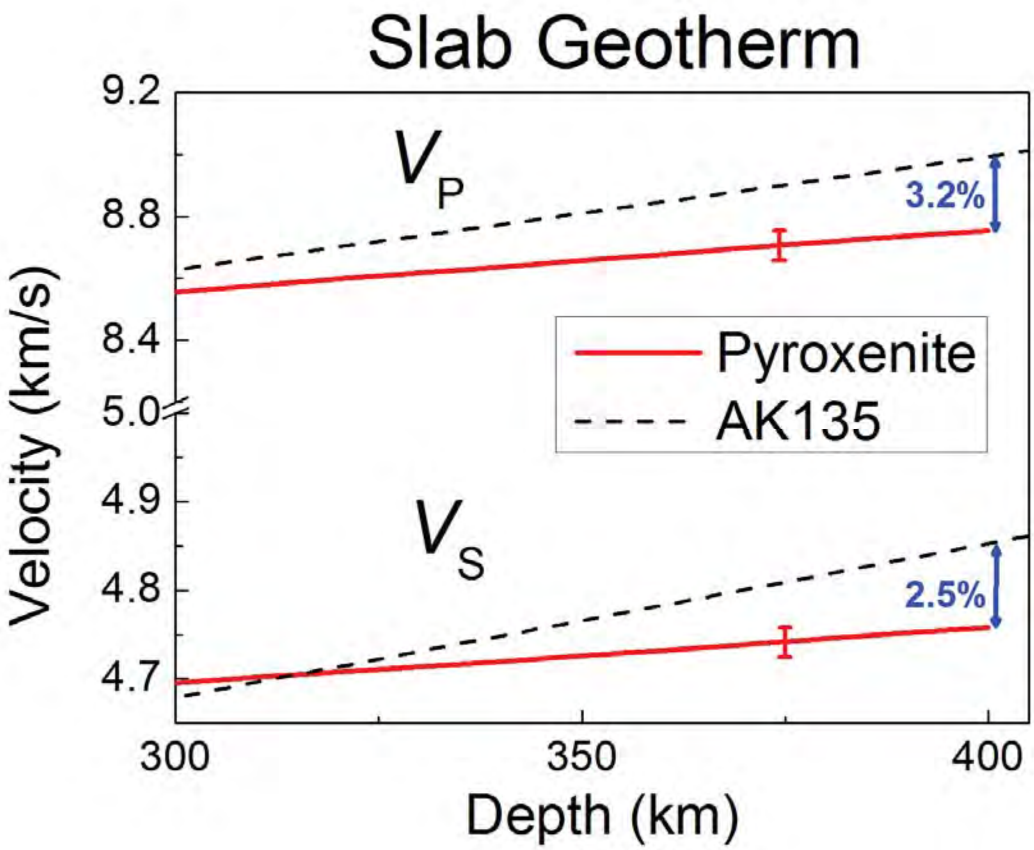
Slab Geotherm
9.2
8.8
8.4
5.0
4.9
4.8
4.7
Velocity (km/s)
V
P
V
S
3.2%
2.5%
Pyroxenite
AK135
300
350
400
Depth (km)

Fig. 10

DOI: https://doi.org/10.2138/am-2020-7075

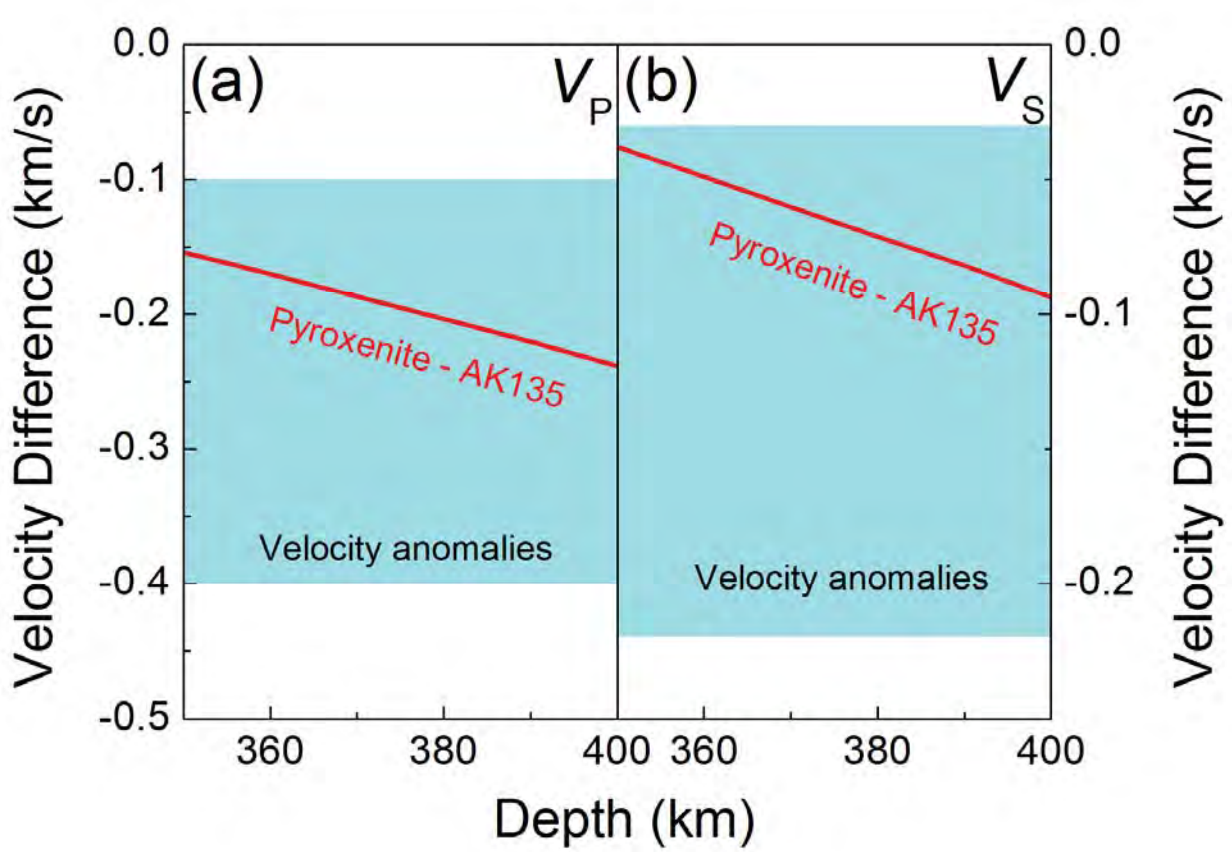

Fig. 11